

1 **Rheologic constraints on the upper mantle from five years of**
2 **postseismic deformation following the El Mayor-Cucapah**
3 **earthquake**

4 **T. T. Hines¹, E. A. Hetland¹**

5 ¹Department of Earth and Environmental Sciences, University of Michigan, Ann Arbor, Michigan, USA.

6 **Key Points:**

- 7 • Transient postseismic deformation can be observed following the El Mayor-Cucapah
8 earthquake at epicentral distances of up to 400 km
9 • Near-field postseismic deformation exhibits early transience that decays to a sustained
10 rate which is elevated above the preseismic trend
11 • Far-field postseismic deformation can be explained with a Zener or Burgers rheology
12 upper mantle

13 **Abstract**

14 We analyze five years of Southern California GPS data following the Mw=7.2 El Mayor-
 15 Cucapah earthquake. We observed transient postseismic deformation which persists for three
 16 years at epicentral distances greater than ~ 200 km. In the near-field, rapid postseismic trans-
 17 sience decays to a sustained rate which exceeds its pre-earthquake trend. We attempt to de-
 18 termine the mechanisms driving this deformation, where we consider afterslip at seismogenic
 19 depths and viscoelastic relaxation in the lower crust and upper mantle as candidate mechanisms.
 20 We find that early, rapid, near-field deformation can be explained with afterslip on the fault
 21 that ruptured coseismically, while the later, sustained, near-field deformation can be explained
 22 with either continued afterslip in an effectively elastic lower crust, or lower crustal viscoelas-
 23 tic relaxation with a steady-state viscosity of $\sim 10^{19}$ Pa s. The trend in far-field deformation
 24 is best explained with a transient viscosity of $\sim 10^{18}$ Pa s in the upper mantle. We argue that
 25 a transient rheology in the mantle is preferable over a Maxwell rheology because it better pre-
 26 dicts the decay in postseismic deformation, and also because it does not conflict with the gen-
 27 erally higher, steady-state viscosities inferred from studies of geophysical processes occurring
 28 over longer time-scales.

29 **1 Introduction**

30 Ground deformation in the years following a large ($Mw \gtrsim 7$) earthquake can be used to
 31 gain insight into the mechanical behavior of the crust and upper mantle. The interpretations
 32 of postseismic deformation are not always conclusive because multiple postseismic deforma-
 33 tion mechanisms, such as afterslip or viscoelastic relaxation in the lower crust and upper man-
 34 tle, can have qualitatively similar surface expressions [e.g. Savage, 1990]. This complication
 35 can potentially be remedied by having a sufficient number of well positioned observations of
 36 the postseismic displacement field [Hearn, 2003]. Owing to the dense geodetic network de-
 37 ployed throughout the 2000s as part of the Plate Boundary Observatory, the postseismic de-
 38 formation following the April 4, 2010, Mw=7.2 El Mayor-Cucapah earthquake in Baja Cal-
 39 ifornia was observed at more GPS stations than any other earthquake in California to date. With
 40 such a large collection of data, we attempt to discern the mechanisms driving postseismic de-
 41 formation following the El Mayor-Cucapah earthquake.

42 Here is some background on the El Mayor Earthquake

43 Previous studies which have modeled postseismic deformation following the El Mayor-
 44 Cucapah earthquake include Pollitz *et al.* [2012], Gonzalez-Ortega *et al.* [2014], Spinler *et al.*
 45 [2015], and Rollins *et al.* [2015]. Of these studies, Gonzalez-Ortega *et al.* [2014] and Rollins
 46 *et al.* [2015] have attempted to describe the postseismic deformation with afterslip in an elas-
 47 tic half-space. Gonzalez-Ortega *et al.* [2014] described five months of postseismic deforma-
 48 tion, observed by InSAR and GPS stations within ~ 50 km of the rupture, with afterslip and
 49 contraction on the coseismically ruptured fault. Gonzalez-Ortega *et al.* [2014] noted that their
 50 preferred model underestimated the GPS displacements for stations $\gtrsim 25$ km from the rup-
 51 ture and suggested that it could be the result of unmodeled viscoelastic relaxation. Using only
 52 continuous GPS stations, which are mostly north of the rupture zone, Rollins *et al.* [2015] found
 53 that three years of postseismic deformation can be adequately explained by afterslip, albeit with
 54 an implausibly large amount of slip inferred on the least constrained, southern-most fault seg-
 55 ment. Here, we suggest the afterslip inferred by Rollins *et al.* [2015] may have been acting as
 56 a proxy for distributed relaxation in the upper mantle.

57 Pollitz *et al.* [2012], Rollins *et al.* [2015] and Spinler *et al.* [2015] have explored viscoelas-
 58 tic relaxation in the lower crust and upper mantle as a potential postseismic deformation mech-
 59 anism. The rheology of the crust and mantle is largely unknown and so modeling postseis-
 60 mic deformation with viscoelastic relaxation requires one to assume a rheologic model and
 61 then find the best fitting rheologic parameters. The inference of these rheologic parameters is
 62 a computationally expensive non-linear inverse problem which is typically approached with

a forward modeling grid search method. Consequently, a simplified structure for the Earth must be assumed in order to minimize the number of rheologic parameters that need to be estimated. For example, it is commonly assumed that the lower crust and upper mantle are homogeneous, Maxwell viscoelastic layers, which may be too simplistic for postseismic studies [Riva and Govers, 2009; Hines and Hetland, 2013]. To further reduce the dimensions of the model space, it is also necessary to make simplifying assumptions about the behavior of afterslip. For example, one can assume a frictional model for afterslip and parametrize afterslip in terms of the unknown rheologic properties of the fault [e.g. Johnson *et al.*, 2009; Johnson and Segall, 2004]. One can also assume that afterslip does not persist for more than a few months and then model the later postseismic deformation assuming it to be the result of only viscoelastic relaxation [e.g. Pollitz *et al.*, 2012; Spinler *et al.*, 2015]. However, postseismic afterslip in similar tectonic settings has been observed to persist for decades following earthquakes [Çakir *et al.*, 2012; Cetin *et al.*, 2014]. Indeed, the preferred viscoelastic model from Pollitz *et al.* [2012] significantly underestimates deformation in the Imperial Valley, which could be indicative of unmodeled continued afterslip. Neglecting to allow for sustained afterslip as a postseismic mechanism could then lead to biased inferences of viscosities.

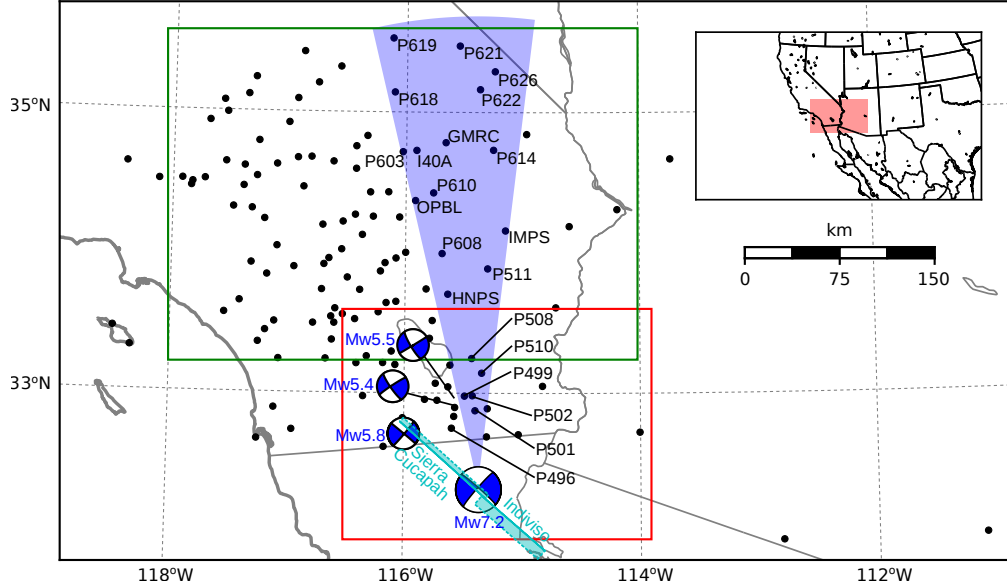
In this study, we perform a kinematic inversion for fault slip, allowing it to persist throughout the postseismic period, while simultaneously estimating the viscosity of the lower crust and upper mantle. We create an initial model of the fault slip and effective viscosity necessary to describe early postseismic deformation using the method described in Hines and Hetland [2016]. This method uses a first-order approximation of surface deformation resulting from viscoelastic relaxation which is only applicable to the early postseismic period. In this case, our initial model describes the first 0.8 years of postseismic deformation following the El Mayor-Cucapah earthquake. We then use the inferred effective viscosity structure from the initial model to create a suite of postseismic models to explain the five years of postseismic data available to date. Of the suite of models tested, we find that postseismic deformation following the El Mayor-Cucapah earthquake can be explained with a combination of afterslip on a fault segment running through the Sierra Cucapah and a Zener rheology in the upper mantle with a transient viscosity on the order of 10^{18} Pa s.

2 Data Processing

We use continuous GPS position time series provided by University Navstar Consortium (UNAVCO) for stations within a 400 km radius about the El Mayor-Cucapah epicenter. We collectively describe the coseismic and postseismic displacements resulting from the El Mayor-Cucapah earthquake as $u_{\text{post}}(t)$. We consider the GPS position time series, $u_{\text{obs}}(t)$, to be the combination of $u_{\text{post}}(t)$, secular tectonic deformation, annual and semi-annual oscillations, and coseismic offsets from significant earthquakes over the time span of this study. The June 14, 2010, Mw=5.8 Ocotillo earthquake and the Brawley swarm, which included an Mw=5.5 and an Mw=5.4 event on August 26, 2012, (Figure 1) are the only earthquakes that produced noticeable displacements in any of the time series. We treat the displacements resulting from the Brawley swarm as a single event because the daily solutions provided by UNAVCO cannot resolve the separate events. Although the Ocotillo earthquake had its own series of aftershocks [Hauksson *et al.*, 2011], neither the Ocotillo earthquake nor the Brawley swarm produced detectable postseismic deformation. We model displacements resulting from these events with only a Heaviside function, $H(t)$, describing the coseismic offsets. We then model $u_{\text{obs}}(t)$ as

$$u_{\text{obs}}(t) = u_{\text{pred}}(t) + \epsilon, \quad (1)$$

where



92 **Figure 1.** Map of the region considered in this study. The large focal mechanism is for the El Mayor-
 93 Cucapah earthquake, and the three small focal mechanisms are for the Ocotillo earthquake and the two main
 94 shocks during the Brawley swarm. The black dots indicate the locations of GPS stations used in this study.
 95 The fault geometry used in this study is shown in cyan where dashed lines indicate buried edges of the fault
 96 segments. The green and red boxes demarcate the extent of the near-field and far-field maps (Figures 4 and 5).
 97 Stations inside the blue sector, which highlights the area within 10° of the El Mayor-Cucapah P axis, are used
 98 in Figures 7 and 10.

$$\begin{aligned} u_{\text{pred}}(t) = & u_{\text{post}}(t)H(t - t_{\text{emc}}) + c_0 + c_1t + \\ & c_2 \sin(2\pi t) + c_3 \cos(2\pi t) + c_4 \sin(4\pi t) + c_5 \cos(4\pi t) + \\ & c_6 H(t - t_{\text{oc}}) + c_7 H(t - t_{\text{bs}}). \end{aligned} \quad (2)$$

115 In the above equations, t_{emc} , t_{oc} and t_{bs} are the times of the El Mayor-Cucapah earthquake,
 116 Ocotillo earthquake, and the Brawley swarm, respectively, c_0 through c_7 are unknown coef-
 117 ficients, and ϵ is the observation noise. We are using years as our unit of time which makes
 118 c_2 through c_5 the coefficients for annual and semi-annual oscillations. We only estimate jumps
 119 associated with the Ocotillo earthquake and Brawley swarm for stations within 40 km of their
 120 epicenters.

121 Stations which recorded displacements that clearly cannot be described by the aforemen-
 122 tioned processes are not included in our analysis. This includes stations in the Los Angeles
 123 basin, where anthropogenic deformation can be larger than the postseismic signal that we are
 124 trying to estimate [Bawden *et al.*, 2001; Argus *et al.*, 2005]. In order to ensure an accurate es-
 125 timation of the secular deformation, we only use stations that were installed at least six months
 126 prior to El Mayor-Cucapah earthquake even though several GPS stations were installed after
 127 the earthquake to get better coverage of the postseismic deformation field [Spinler *et al.*, 2015].
 128 It would be possible to subtract secular velocities derived from elastic block models [e.g. Meade
 129 and Hager, 2005] from velocities recorded at the newly installed stations to get an estimate
 130 of postseismic velocities at those stations. However, estimating velocities from an already noisy
 131 displacement time series can introduce significant uncertainties depending on exactly how the
 132 estimation is done. We therefore use coseismic and postseismic displacements, rather than ve-

133 locities, in our inverse method described in Section 3. This choice prevents us from using the
134 newly installed stations for our analysis.

135 The October 16, 1999, Mw=7.1 Hector Mine earthquake, which occurred \sim 270 km north
136 of the El Mayor-Cucapah epicenter, produced transient postseismic deformation which we do
137 not wish to model, either mechanically or through empirical line fitting. We thus restrict our
138 analysis to deformation observed six years after the Hector Mine earthquake, which is when
139 postseismic velocities at sites near the Hector Mine epicenter are approximately constant [Sav-
140 age and Svare, 2009]. When appraising our model fit in Section 3, we see some systematic
141 residuals in the vicinity of the Hector Mine epicenter, which may be the result of errors in the
142 assumption that the trend in Hector Mine postseismic deformation is linear after six years.

143 Studies of postseismic deformation typically assume a parametric form for $u_{\text{post}}(t)$, such
144 as one with a logarithmic or exponential time dependence [e.g. Savage *et al.*, 2005]. However,
145 by assuming a logarithmic or exponential form of $u_{\text{post}}(t)$ we run the risk of over fitting the
146 GPS time series and inferring a non-existent postseismic signal. We therefore do not assume
147 any parametric form for $u_{\text{post}}(t)$ and rather treat it as integrated Brownian motion, so that

$$\dot{u}_{\text{post}}(t) = \sigma^2 \int_0^t w(s) ds, \quad (3)$$

148 where $w(t)$ is white noise and the variance of $\dot{u}_{\text{post}}(t)$ increases linearly with time by a fac-
149 tor of σ^2 . We use a Kalman filtering approach to estimate $u_{\text{post}}(t)$ and the unknown param-
150 eters in eq. (2). In the context of Kalman filtering, our time varying state vector is

$$\mathbf{X}(t) = [u_{\text{post}}(t), \dot{u}_{\text{post}}(t), c_0, \dots, c_7] \quad (4)$$

151 and eq. (2) is the observation function which maps the state vector to the GPS observations.
152 We initiate the Kalman filter by assuming a prior estimate of $\mathbf{X}(t)$ at the first time epoch, de-
153 noted $\mathbf{X}_{1|0}$, which has a sufficiently large covariance, denoted $\Sigma_{1|0}$, to effectively make our
154 prior uninformed. For each time epoch, t_i , Bayesian linear regression is used to incorporate
155 GPS derived estimates of displacement with our prior estimate of the state, $\mathbf{X}_{i|i-1}$, to form
156 a posterior estimate of the state, $\mathbf{X}_{i|i}$, which has covariance $\Sigma_{i|i}$. We then use the posterior
157 estimate of the state at time t_i to form a prior estimate of the state at time t_{i+1} through the
158 transition function

$$\mathbf{X}_{i+1|i} = \mathbf{F}_{i+1} \mathbf{X}_{i|i} + \delta_{i+1}, \quad (5)$$

159 where

$$\mathbf{F}_{i+1} = \begin{bmatrix} 1 & (t_{i+1} - t_i) & \mathbf{0} \\ 0 & 1 & \mathbf{0} \\ \mathbf{0} & \mathbf{0} & \mathbf{I} \end{bmatrix} \quad (6)$$

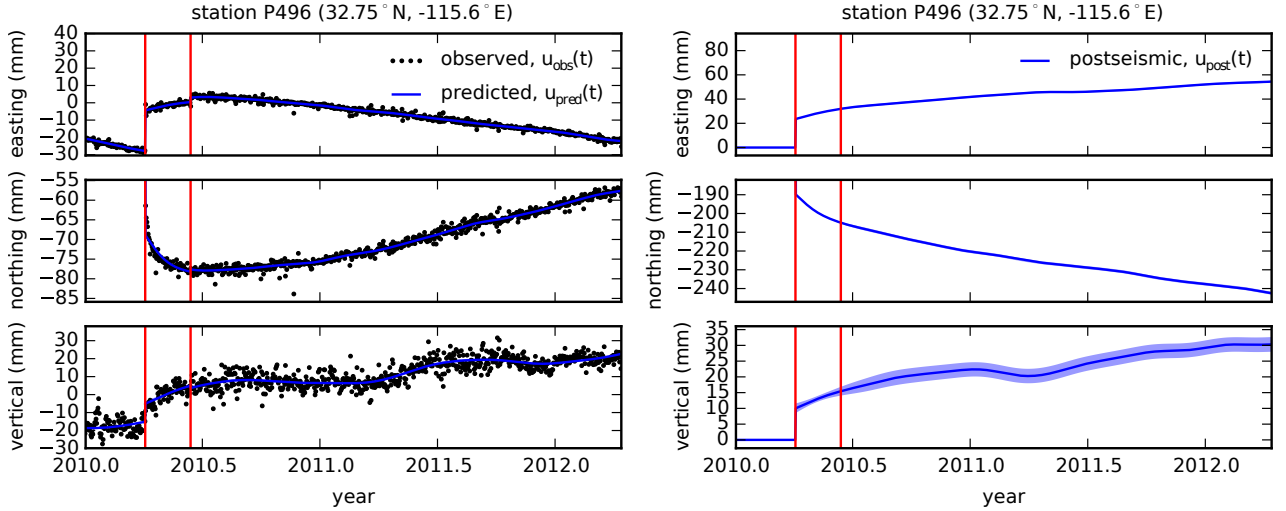
160 and δ_{i+1} is the process noise, which has zero mean and covariance described by

$$\mathbf{Q}_{i+1} = \sigma^2 \begin{bmatrix} \frac{(t_{i+1}-t_i)^3}{3} & \frac{(t_{i+1}-t_i)^2}{2} & \mathbf{0} \\ \frac{(t_{i+1}-t_i)^2}{2} & (t_{i+1} - t_i) & \mathbf{0} \\ \mathbf{0} & \mathbf{0} & \mathbf{0} \end{bmatrix}. \quad (7)$$

161 The covariance of the new prior state, $\mathbf{X}_{i+1|i}$, is then described by

$$\Sigma_{i+1|i} = \mathbf{F}_{i+1} \Sigma_{i|i} \mathbf{F}_{i+1}^T + \mathbf{Q}_{i+1}. \quad (8)$$

162 This process is repeated for each of the N time epochs at which point we use Rauch-Tung-
163 Striebel smoothing [Rauch *et al.*, 1965] to find $\mathbf{X}_{i|N}$, which is an estimate of the state at time

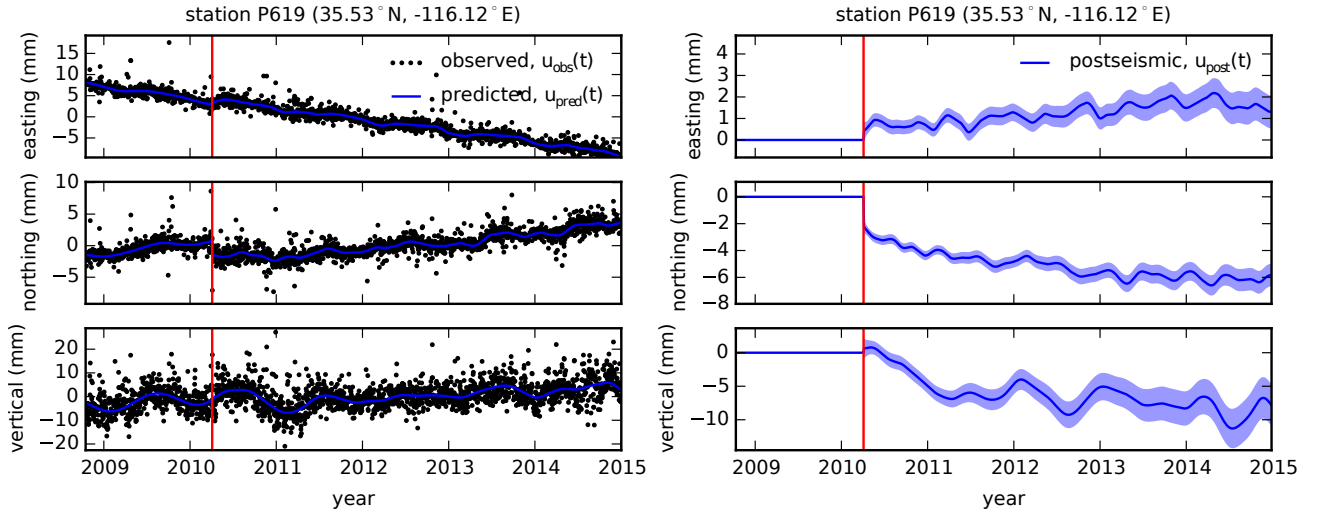


188 **Figure 2.** Left panels show GPS time series from UNAVCO (black) and the predicted displacement (blue)
 189 from eq. (2) for a near-field station. Red lines indicate the times of the El Mayor-Cucapah and Ocotillo earth-
 190 quakes. The right panels show estimated coseismic and postseismic displacements u_{post} which are extracted
 191 from the predicted displacements. The 68% confidence interval is shown in light blue.

164 t_i that incorporates GPS observation for all N time epochs. Our final estimates of $u_{\text{post}}(t)$
 165 are used in subsequent analysis, while the remaining components of the state vector are con-
 166 sidered nuisance parameters. In the interests of computational tractability, we down sample
 167 our smoothed time series from daily solutions down to weekly solutions.

168 The smoothness of $u_{\text{post}}(t)$ is controlled by the chosen value of σ^2 , which describes how
 169 rapidly we expect postseismic displacements to vary over time. Setting σ^2 equal to zero will
 170 effectively result in modeling $u_{\text{post}}(t)$ as a straight line which is insufficient to describe the
 171 expected transient behavior in postseismic deformation. The other end member, where σ^2 is
 172 infinitely large, will result in $u_{\text{pred}}(t)$ over fitting the data. While one can use a maximum like-
 173 lihood based approach for picking σ^2 [e.g. Segall and Mathews, 1997], we instead take a sub-
 174 jective approach and choose a value for σ^2 that is just large enough to faithfully describe the
 175 observed deformation at the most near-field station in our study, P496, which exhibits the most
 176 rapid changes in velocity. This ensures that σ^2 will be sufficiently large so that our estimate
 177 of $u_{\text{post}}(t)$ does not smooth out potentially valuable postseismic signal at the remaining sta-
 178 tions. We find that using $\sigma^2 = 0.05 \text{ m}^2/\text{yr}^3$ adequately describe all but the first week of post-
 179 seismic deformation at station P496, which gets incorporated into our estimate of coseismic
 180 displacements (Figure 2). We assume that the first week of deformation is overwhelmingly the
 181 result of afterslip and this afterslip is lumped into our estimates of coseismic slip. We include
 182 an example of estimating $u_{\text{post}}(t)$ for a far-field station, P619, which is about 359 km from
 183 the El Mayor-Cucapah epicenter (Figure 3). At station P619, along with all the other stations
 184 in the Mojave region, there is a south-trending postseismic transience that persists for the first
 185 three years after the El Mayor-Cucapah earthquake. Postseismic deformation that extends to
 186 these epicentral distances has also been observed after the Hector Mine earthquake [Freed et al.,
 187 2007].

193 It is important to note that the shown uncertainties in $u_{\text{post}}(t)$ do not account for the non-
 194 negligible epistemic uncertainty in eq. (2). For example, we assume a constant rate of secu-
 195 lar deformation, which appears to be an appropriate approximation for all but perhaps the sta-
 196 tions closest to the Hector Mine epicenter, as noted above. Also, our model for seasonal de-
 197 formation in eq. (2) assumes a constant amplitude over time, which means that any yearly vari-
 198 ability in the climatic conditions could introduce systematic residuals [Davis et al., 2012]. In-



192 **Figure 3.** same as Figure 2 but for a far-field station.

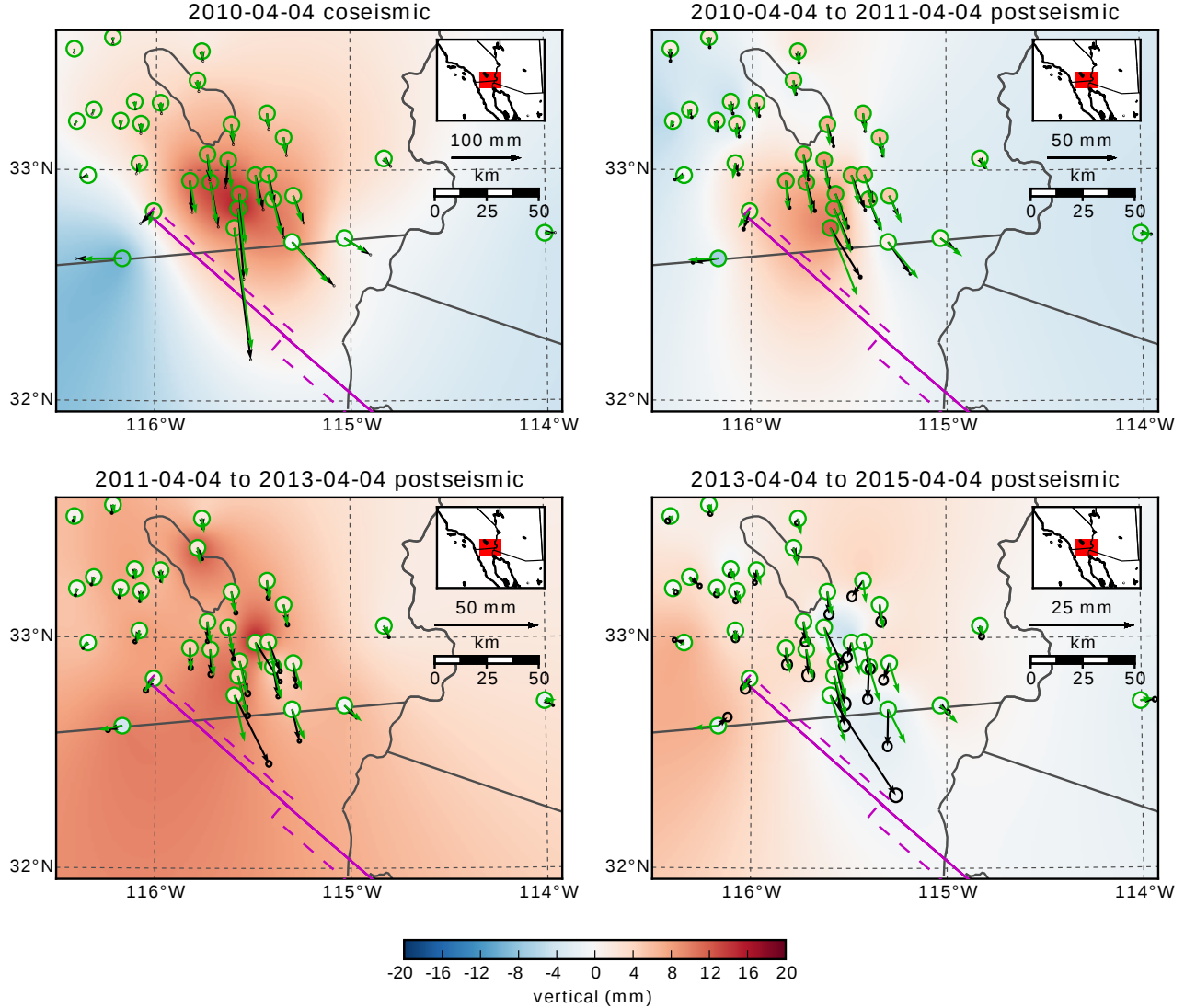
199 indeed, it would be more appropriate to consider the seasonal amplitudes c_2-c_5 in eq. (2) as
200 stochastic variables [Murray and Segall, 2005]. By using constant seasonal amplitudes, our es-
201 timate of $u_{\text{post}}(t)$ seems to describe some of the unmodeled annual and semi-annual oscilla-
202 tions (e.g. Figure 3).

203 We show in Figures 4 and 5 the near and far-field postseismic displacements accumu-
204 lated over the time intervals 0-1 years, 1-3 years, and 3-5 years, as well as the coseismic dis-
205 placements. Stations at epicentral distances beyond ~ 200 km have an elevated rate of defor-
206 mation for the first three years following the earthquake. This far-field deformation is trend-
207 ing southward at a rate of a few millimeters per year along the direction of the El Mayor-Cucapah
208 P axis. A similar eastward trend can be seen in the few far-field stations in Arizona, located
209 along the T axis. After three years, the trend in far-field postseismic deformation is barely per-
210 ceptible. Most far-field stations display an initial subsidence for the first year after the El Mayor-
211 Cucapah earthquake followed by continued uplift. This trend in vertical deformation can be
212 observed in all three of the quadrants where postseismic data is available, which means that
213 the vertical deformation does not exhibit an anti-symmetric quadrant pattern, as would be ex-
214 pected for postseismic processes. Although we use vertical deformation in our analysis in Sec-
215 tion 3, we do not put an emphasis on trying to describe the vertical deformation as it likely
216 does not have postseismic origins.

222 The near-field postseismic deformation is notably sustained when compared to the far-
223 field deformation. Namely, the station in this study which is closest to the El Mayor-Cucapah
224 epicenter, P496, has a steady postseismic trend of ~ 1.5 cm/yr to the south after about one year.
225 Vertical postseismic deformation in the near-field does display a quadrant pattern which is con-
226 sistent with the coseismic vertical deformation, suggesting that it is resulting from postseis-
227 mic processes. However, the vertical postseismic signal is only apparent for the first year af-
228 ter the earthquake (Figure 4). As with the far-field deformation, there is a general trend of up-
229 lift in the near-field after about one year.

230 3 Postseismic Modeling

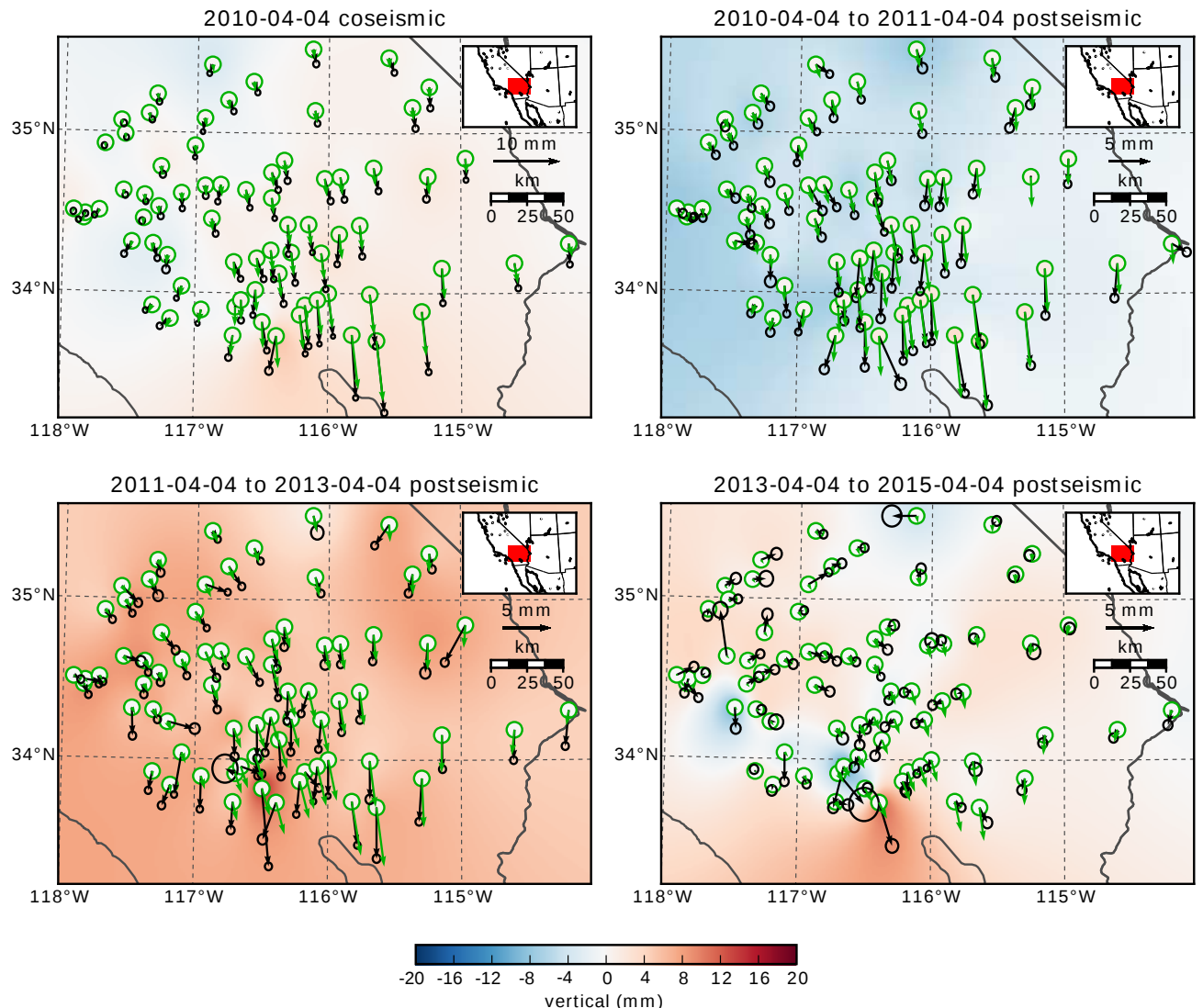
234 We seek to find the mechanisms driving five years of postseismic deformation follow-
235 ing the El Mayor-Cucapah earthquake and we consider afterslip and viscoelastic relaxation as
236 candidate mechanisms. Poroelastic rebound has also been used to model postseismic defor-
237 mation [e.g. Jónsson *et al.*, 2003]; however, Gonzalez-Ortega *et al.* [2014] found that poroe-



217 **Figure 4.** Near-field coseismic and cumulative postseismic displacements over the indicated time periods
 218 (black) as well as predicted displacements for our preferred model from Section 3.3 (green). Observed vertical
 219 deformation is shown as an interpolated field and predicted vertical displacements are shown within the
 220 green circles. Note that the interpolant is not well constrained in Mexico where there is no data available.

depth (km)	λ (GPa)	μ (GPa)	η_{eff} (10^{18} Pa s)	μ_k/μ
0-5	24.0	24.0	-	-
5-15	35.0	35.0	-	-
15-30	42.0	42.0	44.3	0.0
30-60	61.0	61.0	5.91	0.375
60-90	61.0	61.0	1.99	0.375
90-120	61.0	61.0	1.31	0.375
120-150	61.0	61.0	1.10	0.375
150- ∞	61.0	61.0	1.07	0.375

231 **Table 1.** Assumed and estimated material properties. λ and μ are assumed known *a priori* and are based
 232 on the values used for the coseismic model by Wei *et al.* [2011b]. The values for η_{eff} are estimated in Section
 233 3.2, and μ_k/μ are the optimal shear moduli ratios found in Section 3.3 for a Zener rheology upper mantle.

**Figure 5.** Same as Figure 4 but for far-field stations.

lastic rebound is unlikely to be a significant contributor to postseismic deformation following the El Mayor-Cucapah earthquake. Furthermore, we consider stations which are sufficiently far away from the main rupture that poroelastic rebound should be insignificant.

We estimate coseismic and time-dependent postseismic fault slip, both of which are assumed to occur on a fault geometry modified from *Wei et al.* [2011b]. Field studies [*Fletcher et al.*, 2014] and LIDAR observations [*Oskin et al.*, 2012] have revealed a significantly more complicated fault geometry than what was inferred by *Wei et al.* [2011b], especially within the Sierra Cucapah. However, we find that a relatively simple coseismic fault geometry based on [*Wei et al.*, 2011b] is adequate because most of the stations used in this study are sufficiently far from the El Mayor-Cucapah rupture zone that they are insensitive to the details in the fault geometry found by *Fletcher et al.* [2014] and *Oskin et al.* [2012]. The fault geometry used in this study (Figure 1) consists of the two main fault segments inferred by *Wei et al.* [2011b], where the northern segment runs through the Sierra Cucapah up to the US-Mexico border and the southern segment is the Indiviso fault which extends down to the Gulf of California. Both segments extend from the surface to 15 km depth. We extend the northern segment by 40 km to the north-west, motivated by the clustering of aftershocks on the northern tip of the coseismic rupture zone [*Hauksson et al.*, 2011; *Kroll et al.*, 2013]. This extended fault segment was also found to be necessary by *Rollins et al.* [2015] and *Pollitz et al.* [2012] in order to describe the postseismic deformation.

3.1 Elastic Postseismic Inversion

We consider a variety of rheologic models for the lower crust and upper mantle. The simplest rheologic model is to consider them to be effectively elastic and isotropic. In such case, the rheologic parameters consist of the Lamé parameters, λ and μ , which are reasonably well known and we use the same values used by *Wei et al.* [2011b] throughout this paper (Table 1). The only unknown is the distribution of fault slip, which can be easily estimated from postseismic deformation through linear least squares. Using a subset of the GPS stations considered in this study, *Rollins et al.* [2015] found that three years of postseismic deformation following the El Mayor-Cucapah earthquake can be explained with afterslip on the coseismic fault plane without requiring any viscoelastic relaxation. We also perform an elastic slip inversion, but we use GPS stations within a larger radius about the El Mayor-Cucapah epicenter (400 km instead of \sim 200 km). Our forward problem describing predicted postseismic deformation u_{pred} in terms of time dependent fault slip, s , is

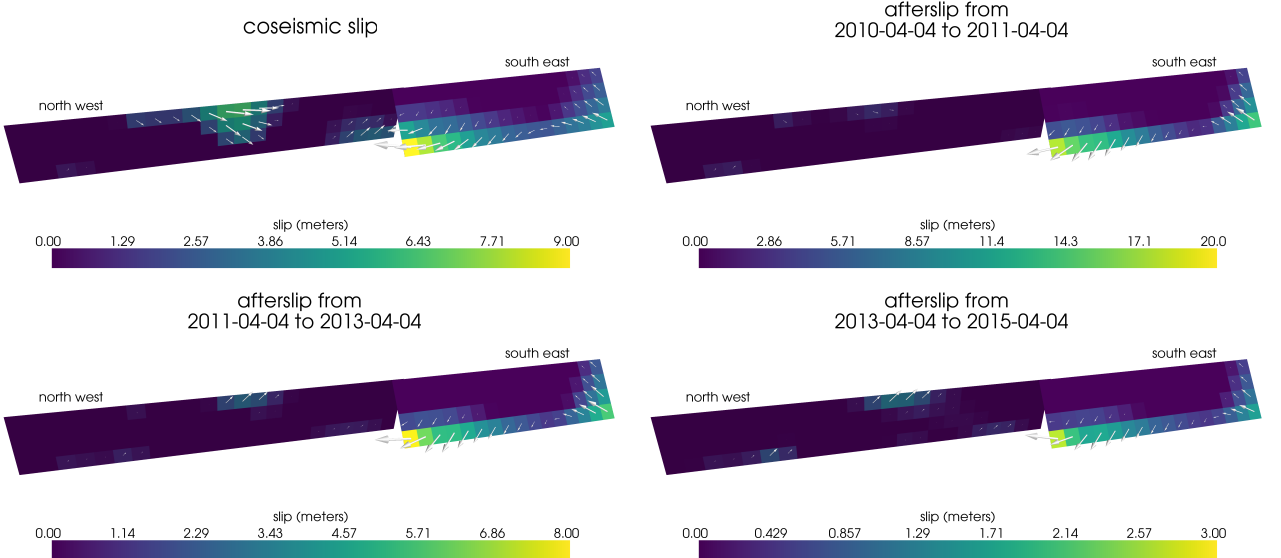
$$u_{\text{pred}}(x, t) = \int_F s(\xi, t) g(x, \xi) d\xi, \quad (9)$$

where F denotes the fault and $g(x, \xi)$ is the elastic Green's function describing displacement at surface position x resulting from slip at ξ on the fault. We estimate coseismic slip and the rate of afterslip over the time intervals 0.0-0.125, 0.125-0.25, 0.25-0.5, 0.5-1.0, 1.0-2.0, 2.0-3.0, 3.0-4.0, and 4.0-5.0 years after the earthquake. Each fault segment is discretized into roughly 4 km by 4 km patches and we estimate a strike-slip and dip component of slip for each patch. We impose that the direction of slip and slip rate are within 45° of right-lateral. We also add zeroth-order Tikhonov regularization so that our solution for s satisfies

$$\min_s \left(\left\| \frac{u_{\text{pred}}(s) - u_{\text{post}}}{\sigma_{\text{post}}} \right\|_2^2 + \lambda_s \|s\|_2^2 \right), \quad (10)$$

where σ_{post} is the uncertainty on postseismic displacements and λ_s is a penalty parameter which is chosen with a trade-off curve. We use Pylith [*Aagaard et al.*, 2013] to compute the Green's functions for this inversion as well as for the remaining inversions in this paper.

Our coseismic slip and afterslip solutions are shown in Figure 6. As with *Rollins et al.* [2015], we find that a large amount of afterslip on the Indiviso fault segment is required to



296 **Figure 6.** Coseismic slip and cumulative afterslip over the indicated intervals for the elastic model from
297 Section 3.1. Color indicates the magnitude of slip while arrows indicate the motion of the hanging wall.

282 explain the observations. The potency of our inferred coseismic slip is $3.2 \times 10^9 \text{ m}^3$, equiv-
283 alent to a $M_w=7.28$ earthquake when assuming a shear modulus of 32 GPa. The potency of
284 our inferred cumulative five years of afterslip is $6.1 \times 10^9 \text{ m}^3$, equivalent to a $M_w=7.46$ earth-
285 quake, which is unrealistically large if we consider afterslip to be driven by coseismically in-
286 duced stresses. Figure 7 shows the time series for the observed and predicted postseismic dis-
287 placements at stations along the El Mayor-Cucapah P axis. We show the radial component of
288 displacements with respect to the El Mayor-Cucapah epicenter and we also rescale the dis-
289 placements so that the difference between the minimum and maximum observed displacements
290 are the same for each station. Our elastic slip model accurately describes near-field postseis-
291 mic deformation and systematically underestimates postseismic deformation at epicentral dis-
292 tances $\gtrsim 150$ km. When the fault segments used in the inversion are extended down to 30 km
293 depth, rather than 15 km, the systematic far-field residuals are smaller but remain apparent.
294 Because an elastic model requires an unrealistic amount of afterslip and is unable to predict
295 far-field deformation, we move on to consider viscoelastic models in the next section.

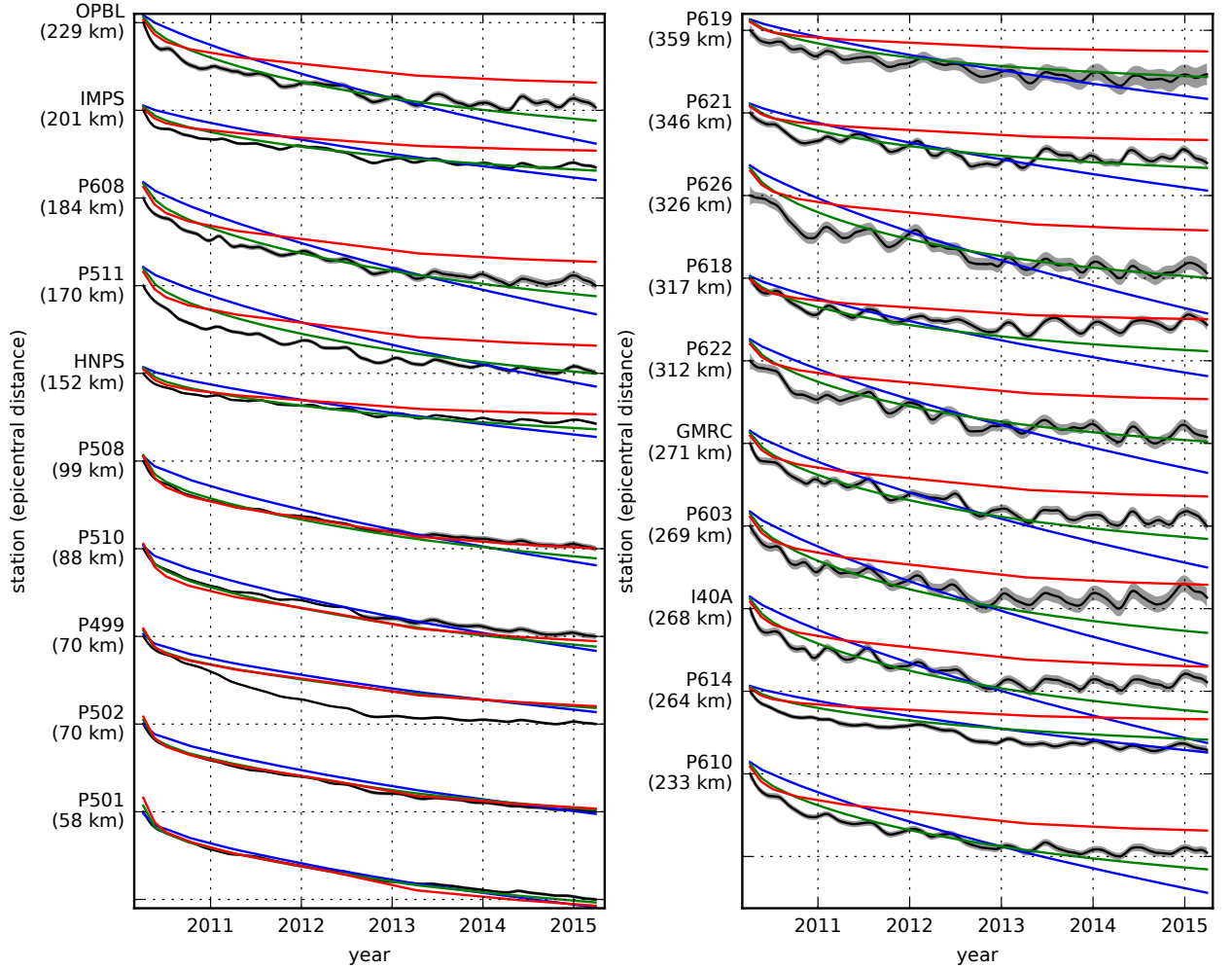
307 3.2 Early Postseismic Inversion

308 For any linear viscoelastic rheology of the crust and mantle, postseismic displacements
309 resulting from time dependent fault slip can be described as

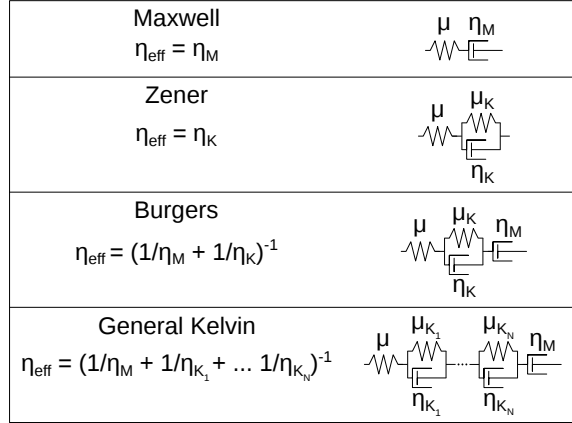
$$u_{\text{pred}}(x, t) = \int_F s(\xi, t) g(x, \xi) d\xi + \int_0^t \int_F s(\xi, \tau) f(t - \tau, x, \xi) d\xi d\tau, \quad (11)$$

310 where $f(t, x, \xi)$ describes the time-dependent velocity at x resulting from viscoelastic relax-
311 ation of stresses induced by slip at ξ . f is a function of λ , μ , and any additional rheologic pa-
312 rameters controlling the viscoelastic response, which are generally not well known. Schematic
313 representations of the viscoelastic rheologic models considered in this study are shown in Fig-
314 ure 8. We discuss these rheologic models and their use in geophysical studies in Section 4.

317 In order to greatly simplify the inverse problem, we use the method described in *Hines*
318 and *Hetland* [2016] to constrain an initial effective viscosity structure from the early postseis-



298 **Figure 7.** Scaled radial component of postseismic displacements. Downward motion indicates that the
 299 station is moving toward the El Mayor-Cucapah epicenter. Displacement time series are scaled so that the
 300 minimum and maximum observed values lie on the grid lines. The observed postseismic displacements, u_{post}
 301 are shown in black with gray indicating the 68% confidence interval. The displacements predicted by the best
 302 fitting elastic model u_{pred} are shown in red. The blue and green lines are the predicted postseismic displace-
 303 ments for the models discussed in Section 3.3. The blue lines show the predicted displacements for the model
 304 with a Maxwell viscoelastic lower crust and upper mantle. The green line shows the predicted displacements
 305 for the model with a Maxwell viscoelastic lower crust and a Zener viscoelastic upper mantle. The effective
 306 viscosities are the same for both models and are shown in Figure 12.



315 **Figure 8.** Schematic illustration of the rheologic models considered in this paper as well as their effective
 316 viscosities.

319 mic deformation. Our method uses the fact that coseismic stresses throughout the crust and
 320 upper mantle depend on the instantaneous elastic parameters and are independent of the viscoelastic
 321 parameters which we wish to estimate. Immediately following an earthquake, each
 322 parcel will have a strain rate that is proportional to the coseismic stress and inversely proportional
 323 to the parcel's effective viscosity, η_{eff} . Using one-dimensional rheologic models, we define the effective
 324 viscosity as

$$\eta_{\text{eff}} = \left. \frac{\sigma}{\dot{\epsilon}} \right|_{t=0}, \quad (12)$$

325 where σ is an applied stress at $t = 0$ and $\dot{\epsilon}$ is the resulting strain rate. Figure 8 shows how
 326 η_{eff} relates to the parameters for various linear viscoelastic rheologies. We can deduce that the
 327 initial rate of surface deformation resulting from viscoelastic relaxation is a summation of the
 328 surface deformation resulting from relaxation in each parcel, scaled by the reciprocal of the
 329 parcel's effective viscosity. That is to say

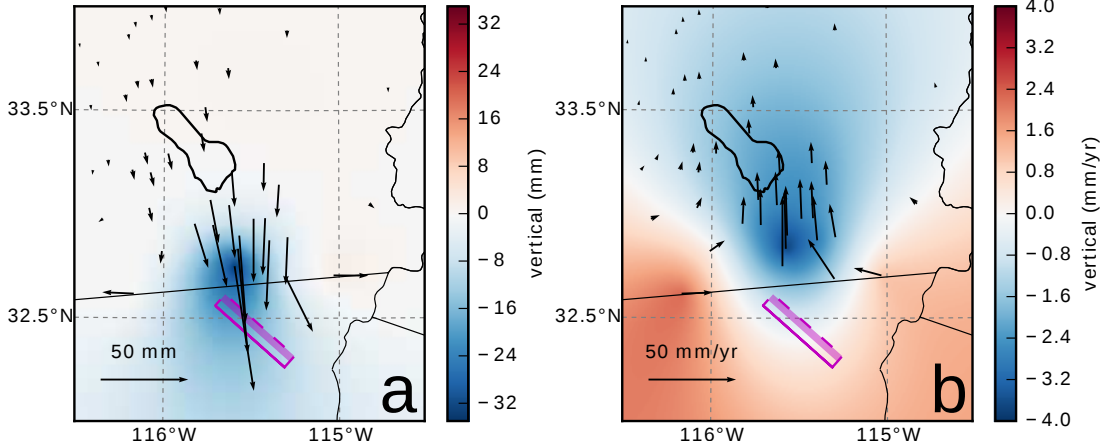
$$f(0, x, \xi) = \int_L \frac{h(x, \xi, \zeta)}{\eta_{\text{eff}}(\zeta)} d\zeta, \quad (13)$$

330 where L denotes the crust and mantle and $h(x, \xi, \zeta)$ describes the initial rate of deformation
 331 resulting from viscoelastic relaxation at ζ induced by slip at ξ . We can combine eq. (13) with
 332 eq. (11) to get a first order approximation for early postseismic deformation,

$$u_{\text{pred}}(x, t) \approx \int_F s(\xi, t) g(x, \xi) d\xi + \int_0^t \int_F \int_L \frac{s(\tau, \xi)}{\eta_{\text{eff}}(\zeta)} h(x, \xi, \zeta) d\zeta d\xi d\tau, \quad (14)$$

333 which is valid for as long as the rate of deformation resulting from viscoelastic relaxation is
 334 approximately constant. Although eq. (14) may only be valid for a short portion of the post-
 335 seismic period, its utility becomes apparent when noting that g and h are only functions of
 336 the fault geometry and instantaneous elastic properties, λ and μ , and thus g and h can be com-
 337 puted numerically as a preprocessing step. The forward problem in eq. (14) can then be rapidly
 338 evaluated for any realization of s and η_{eff} . This is in contrast to evaluating the full forward
 339 problem, eq. (11), numerically for each realization of s and the unknown rheologic proper-
 340 ties.

341 Details on how eq. (14) is used to estimate s and η_{eff} from postseismic deformation can
 342 be found in *Hines and Hetland [2016]*. A non-linear Kalman filter based inverse method can
 343 also be used to estimate s and η_{eff} in a manner akin to *Segall and Mathews [1997]* or *McGuire*



371 **Figure 9.** Displacements resulting from fault slip at lower crustal depths (a), and initial velocities resulting
 372 from subsequent relaxation of a viscoelastic lower crust (b). The fault segment dips 75° to the north-east and
 373 its surface projection is outlined in magenta. The highlighted area on the fault extends from 15 to 30 km depth
 374 and indicates where 1 meter of right-lateral slip was imposed. The elastic properties of the crust and mantle
 375 are the same as in Table 3, and η_{eff} is 10^{18} Pa s in the lower crust. Vertical displacements are interpolated
 376 between station locations.

344 and Segall [2003], in which we would not have to explicitly impose a time dependent parametriza-
 345 tion of s . We have thoroughly explored Kalman filter based approaches, but we ultimately pre-
 346 fer the method described in Hines and Hetland [2016] because of its relative simplicity. More-
 347 over, we believe the piecewise continuous representation of slip with respect to time to be suf-
 348 ficiently general for the resolving power of these GPS data.

349 We estimate coseismic slip and afterslip with the same spatial and temporal discretization
 350 as in Section 3.1. Simultaneously, we estimate η_{eff} within six vertically stratified layers
 351 which have depths ranging from 15-30 km, 30-60 km, 60-90 km, 90-120 km, 120-150 km,
 352 as well as from 150 km to the bottom of our numerical model domain at 800 km. We again
 353 restrict fault slip to occur between 0 and 15 km depth, which is done in order to help elim-
 354 inate inevitable non-uniqueness in the inversion. It has long been recognized that fault slip at
 355 sufficiently great depths can produce surface deformation that is indistinguishable from vis-
 356 coelastic relaxation, at least in two-dimensional earthquake models [Savage, 1990]. Addition-
 357 ally, we note that when simultaneously estimating both afterslip and viscosity in the lower crust,
 358 the inverse problem becomes particularly ill-posed. This ill-posedness is illustrated in Figure
 359 9, which shows the displacements resulting from a meter of slip on a fault extending from 15
 360 to 30 km depth and the initial velocity resulting from subsequent viscoelastic relaxation in the
 361 lower crust, which is given a viscosity of 10^{18} Pa s. In this demonstration, the viscoelastic re-
 362 laxation is entirely driven by the fault slip in the lower crust. The horizontal displacements
 363 from fault slip are in the opposite direction as the displacements resulting from viscoelastic
 364 relaxation. This means that surface displacements resulting from afterslip at lower crustal depths
 365 can be cancelled out, at least partially, by a low viscosity lower crust. We eliminate this null
 366 space by allowing only one mechanism in the lower crust, which we choose to be viscoelas-
 367 tic relaxation. This is not to say that we do not believe deep afterslip to be a possibility; rather,
 368 we restrict slip to seismogenic depths as a modeling necessity. Although, it has been noted
 369 that the pattern of vertical postseismic deformation following the El Mayor-Cucphuong earthquake
 370 indicates that a significant amount of afterslip must be shallow [Rollins et al., 2015].

377 We must determine at which point the early postseismic approximation breaks down, which
 378 we will denote as t_{bd} . As noted, eq. (14) is valid for approximately as long as the rate of de-

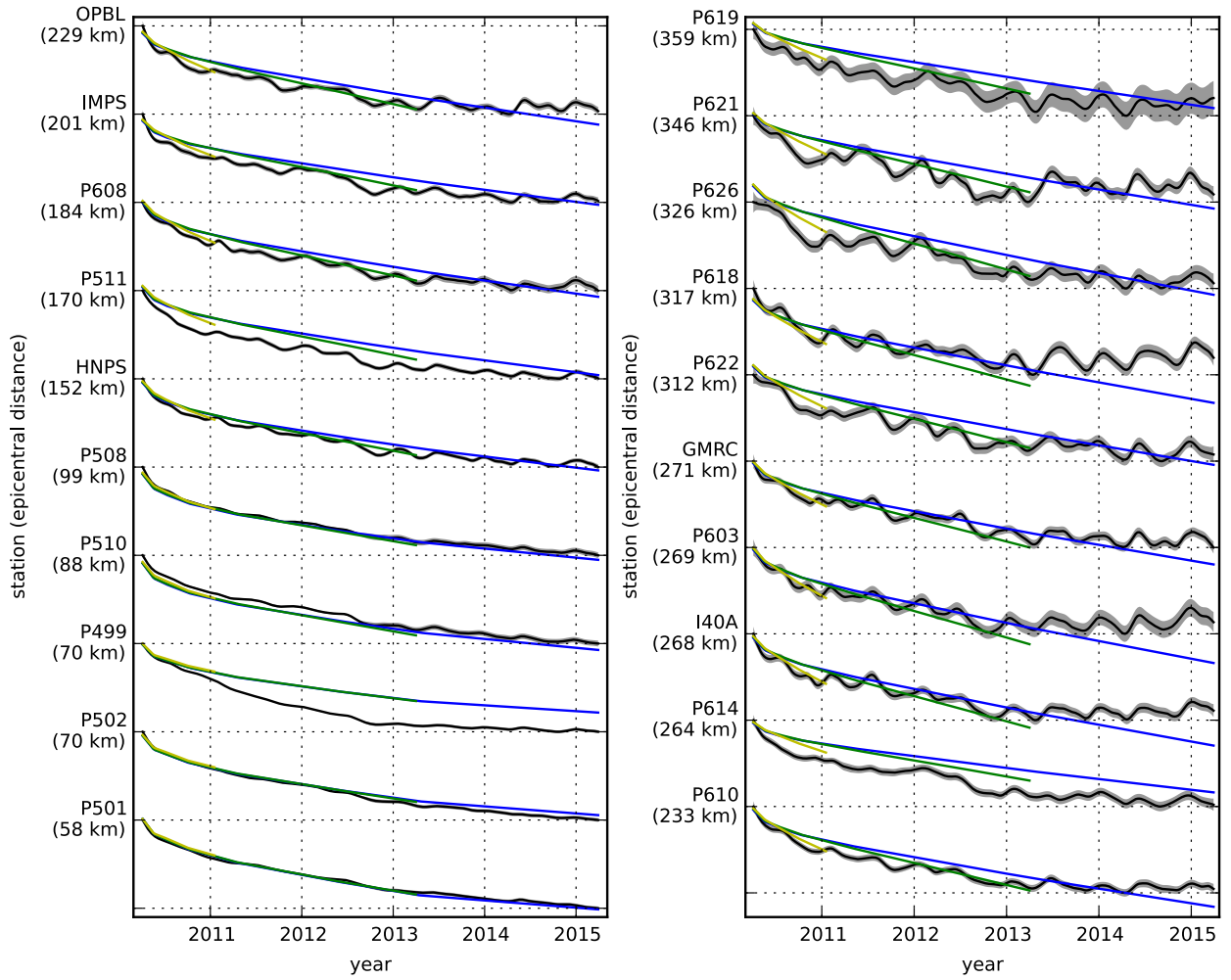
formation resulting from viscoelastic relaxation is approximately constant. We can almost certainly assume that deformation at the most far-field stations, which are ~ 400 km away from the El Mayor-Cucapah epicenter, is the result of viscoelastic relaxation. The approximation should then be valid for as long as a linear trend adequately approximates the far-field deformation. Using this logic, it would appear that t_{bd} is about one year after the El Mayor-Cucapah earthquake. Another way to determine t_{bd} is to find the best fitting prediction of eq. (14) to observed deformation using increasing durations of the postseismic time series. t_{bd} should be the point when eq. (14) is no longer capable of describing the observed deformation without incurring systematic misfits. When using eq. (14) to fit the entire five years of postseismic displacements, we see that the near-field displacements (e.g., station P501) are accurately predicted. When looking at displacements in the far-field (e.g., station P621), we see that eq. (14) overestimates the rate of deformation in the later postseismic period and underestimates the rate of deformation in the early period (Figure 10). Due to the low signal-to-noise ratios for far-field stations, it is difficult to determine at what point eq. (14) is no longer able to predict the observed displacements; however, we settle on $t_{bd} = 0.8$ years after the earthquake, while acknowledging that the choice is subjective. As noted in *Hines and Hetland* [2016], overestimating t_{bd} will result in a bias towards overestimating η_{eff} , while picking a t_{bd} which is too low will not necessarily result in a biased estimate of η_{eff} , although the uncertainties would be larger. We can then consider inferences of η_{eff} to be an upper bound on the viscosity needed to describe the far-field rate of deformation during the first 0.8 years of postseismic deformation.

We estimate coseismic slip, afterslip, and effective viscosities by solving

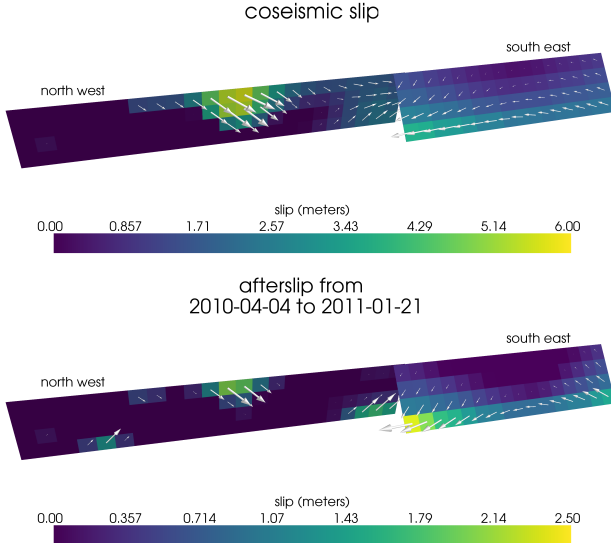
$$\min_{s, \eta_{eff}} \left(\left\| \frac{u_{pred}(s, \eta_{eff}) - u_{post}}{\sigma_{post}} \right\|_2^2 + \lambda_s \|s\|_2^2 + \lambda_\eta \|\nabla \eta_{eff}^{-1}\|_2^2 \right), \quad (15)$$

where u_{post} consists of the first 0.8 years of postseismic deformation and u_{pred} are the predicted displacements from eq. (14). Due to inherent non-uniqueness, we have added zeroth-order Tikhonov regularization to estimates of s and second-order Tikhonov regularization to estimates of effective fluidity η_{eff}^{-1} . The degree to which we impose the regularization on slip and fluidity is controlled by the penalty parameters λ_s and λ_η , which are chosen with trade-off curves (Figure S1). Our goal here is to get a prior constraint on η_{eff} to minimize the amount of searching we have to do when describing the postseismic deformation over the full five years, which we do in Section 3.3. Estimates of s made here will not be used in Section 3.3, and so the motivation behind adding regularization to s is to ensure that the slip driving viscoelastic relaxation in eq. (14) is sensible.

Our initial estimate for coseismic slip and cumulative afterslip over the first 0.8 years after the El Mayor-Cucapah earthquake are shown in Figure 11. Similar to our elastic slip model from Section 3.1, a significant amount of right-lateral and normal coseismic slip is inferred to be on the Sierra Cucapah segment. Our coseismic slip solution on the Sierra Cucapah segment is consistent with field studies [*Fletcher et al.*, 2014] and the model from *Wei et al.* [2011b]. Our inferred slip on the Indiviso fault segment differs from *Wei et al.* [2011b] because the GPS data used in this study is not capable of resolving the spatial distribution of fault slip on that segment (Figure S2). The potency of inferred coseismic slip is $3.3 \times 10^9 \text{ m}^3$, which is also about the same as that inferred from Section 3.1. The present inference of afterslip on the Indiviso fault is significantly less than what was found in the Section 3.1 where we did not account for viscoelasticity. When fault slip is simultaneously estimated with viscosity, the potency of inferred afterslip over the first 0.8 years after the earthquake is $0.85 \times 10^9 \text{ m}^3$, compared to $3.5 \times 10^9 \text{ m}^3$ when we assume the crust and upper mantle are elastic. The significant amount of afterslip inferred on the Indiviso fault seems to be compensating for unmodeled viscoelastic relaxation at depths greater than 60 km. The fact that there is still an appreciable amount of afterslip inferred on the Indiviso fault raises the question of whether it is compensating for viscoelastic relaxation that is more localized than what we allow for since we only estimate depth dependent variations in viscosity.



400 **Figure 10.** Observed postseismic displacements (black) and best fitting predictions of eq. (14) to 5.0 (blue),
401 3.0 (green), and 0.8 (yellow) years of the postseismic data.

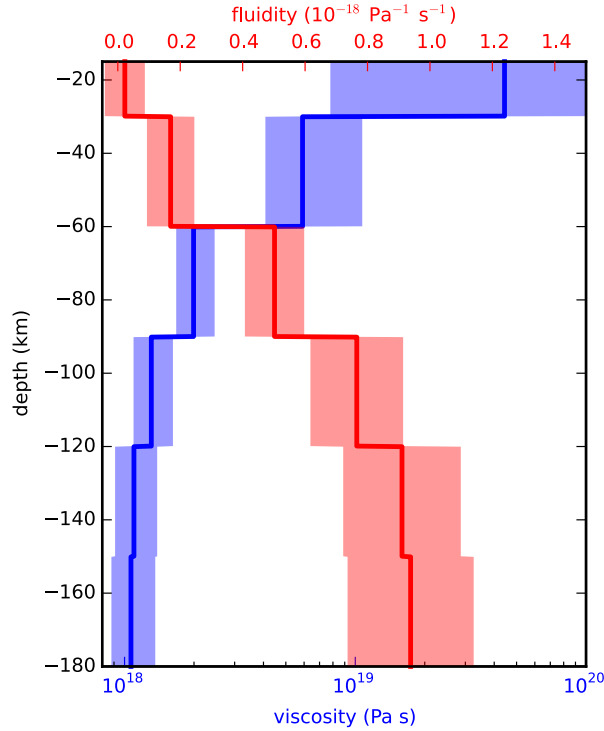


452 **Figure 11.** Coseismic slip and afterslip inferred by fitting eq. (14) to the first 0.8 years of postseismic
453 displacements.

431 Our estimated effective viscosities, and corresponding fluidities, are shown in Figure 12.
432 Although fluidity is rarely used in geophysical literature, eq. (13) is linear with respect to flu-
433 idity and so the fluidity indicates the amplitude of the viscoelastic signal coming from each
434 layer. We use bootstrapping to find the 95% confidence intervals for our estimated effective
435 viscosities which are shown in Figure 12. It is important to remember that the presented ef-
436 fective viscosities were estimated with a smoothing regularization constraint and so the un-
437 certainty are almost certainly underestimated [Aster *et al.*, 2011]. The uncertainties are shown
438 to give the reader a sense of the relative confidence between layers. Indeed, many viscosity
439 profiles which are outside of the shown confidence intervals can just as adequately described
440 the first 0.8 years of postseismic deformation. The solution in (Figure 12) should be interpreted
441 as the smoothest effective viscosity profile which is capable of describing the data. This means
442 that any sharp viscosity transitions will be tapered out, which we demonstrate with a synthetic
443 test in Figure S2. Nonetheless, a robust feature that we see is that the largest jump in fluid-
444 ity is at 60 km depth, which is consistent with the range of lithosphere-asthenosphere bound-
445 ary depths inferred by Lekic *et al.* [2011]. This transitional depth is also consistent with the
446 the viscosity structure required to explain far-field postseismic deformation following the Hec-
447 tor Mine earthquake [Freed *et al.*, 2007]. We find that the viscosity below 60 km depth needs
448 to be $\sim 10^{18}$ Pa s to describe the early rate of postseismic deformation at far-field stations while
449 the lower crust and uppermost mantle need to be relatively stronger. The viscosity of the lower
450 crust is the least well constrained because there is no evidence of relaxation in that layer, mean-
451 ing that it is effectively elastic over the first 0.8 years after the earthquake.

457 3.3 Full Postseismic Inversion

458 In the previous section, we used the inverse method from *Hines and Hetland* [2016] to
459 constrain the effective viscosity structure required to explain the first 0.8 years of postseismic
460 deformation. In this section, we use these effective viscosities as a prior constraint when search-
461 ing for models which are capable of describing the available five years of postseismic data,
462 where our forward problem is now eq. (11) rather than the approximation given by eq. (14).
463 We perform a series of fault slip inversions assuming a variety of rheologies for the lower crust



454 **Figure 12.** Effective viscosities and associated fluidities inferred by fitting eq. (14) to the first 0.8 years of
 455 postseismic displacements. 95% confidence intervals, estimated from bootstrapping, are indicated by color
 456 fields.

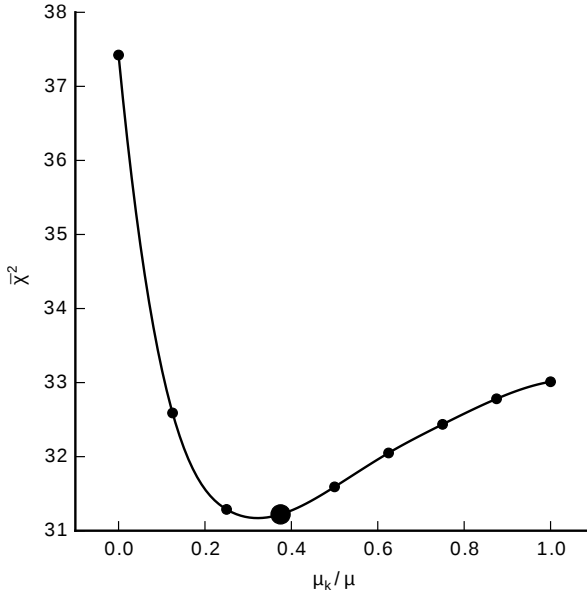
464 and upper mantle which are consistent with our findings from Section 3.2. We appraise each
 465 model using the mean chi-squared value,

$$\bar{\chi}^2 = \frac{1}{N} \left\| \frac{u_{\text{pred}} - u_{\text{post}}}{\sigma_{\text{post}}} \right\|_2^2, \quad (16)$$

466 where N is the number of observations.

467 We first assume that the crust and mantle can be described with a Maxwell rheology,
 468 and we set the steady-state viscosity, η_M , equal to our inference of η_{eff} . We compute f and
 469 g from eq. (11) using Pylith, and we use the same spatial and temporal discretization of s as
 470 in Sections 3.1 and 3.2. We estimate s using linear least squares and find a misfit of $\bar{\chi}^2 =$
 471 37.4. For comparison, $\bar{\chi}^2 = 35.3$ for the elastic model from Section 3.1. The Maxwell vis-
 472 coelastic model has a larger misfit because it tends to overestimate the rate of deformation af-
 473 ter about three years (Figure 7). Since our initial estimates of η_{eff} may be biased towards over-
 474 estimating viscosities, we have also performed the slip inversion where we use uniformly lower
 475 viscosities in the crust and mantle. However, decreasing the viscosity only increases the mis-
 476 fit. Although, the viscosities used here are consistent with the successful Maxwell viscoelas-
 477 tic models found by *Rollins et al.* [2015] and *Spinler et al.* [2015], which had mantle viscosi-
 478 ties on the order of 10^{18} Pa s and relatively higher lower crustal viscosities, we find that such
 479 a model is incapable of describing the entire postseismic time series. *Pollitz et al.* [2001] sim-
 480ilarly recognized this deficiency in a Maxwell rheology, which then motivated their exploration
 481 of a Burgers rheology upper mantle [*Pollitz*, 2003].

482 Instead of exploring a Burgers rheology mantle, which introduces two new parameters
 483 that need to be estimated, the transient viscosity, η_K , and transient shear modulus, μ_K , we first

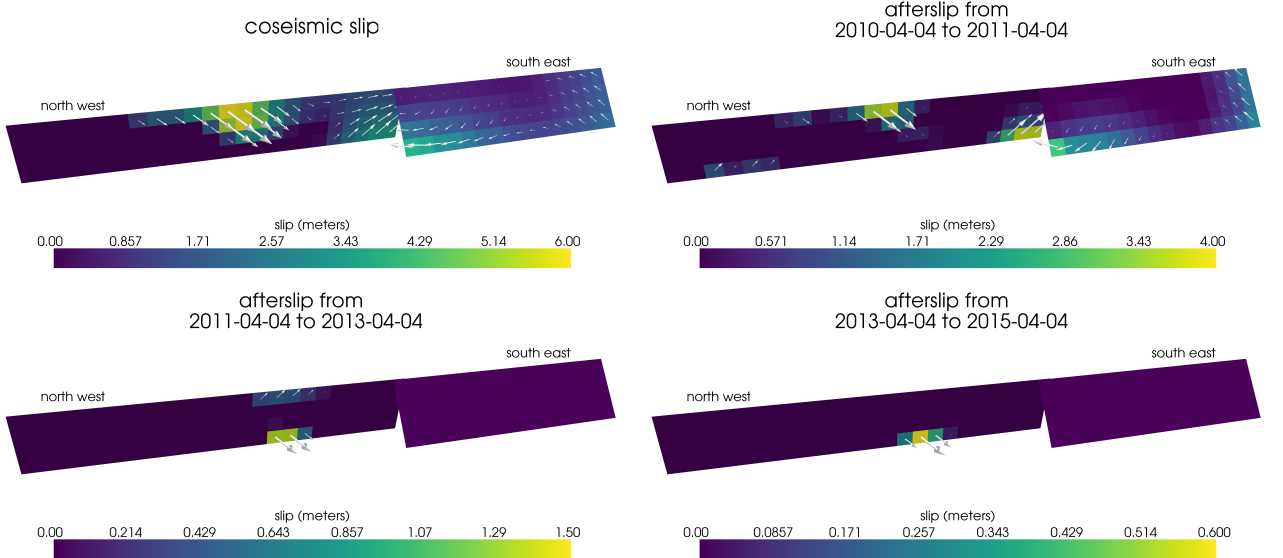


496 **Figure 13.** Mean chi-squared value for the best fitting slip model as a function of the transient shear modu-
 497 lus relative to the elastic shear modulus in a Zener upper mantle. Large dot indicates our preferred ratio.

484 consider a Zener rheology for the mantle, which only introduces one additional unknown pa-
 485 rameter, μ_K . We assume that the lower crust still has a Maxwell rheology. The steady-state
 486 viscosity in the crust and the transient viscosity in the mantle are set equal to the inferred ef-
 487 fective viscosities. We then estimate the ratio of shear moduli, $\frac{\mu_K}{\mu}$. We compute nine differ-
 488 ent sets of Green's functions, f and g , where we assume values of $\frac{\mu_K}{\mu}$ ranging from 0 to 1.
 489 The former being a degenerate case where the Zener model reduces to the above Maxwell model.
 490 We estimate coseismic slip and afterslip for each realization of $\frac{\mu_K}{\mu}$. We find that a shear mod-
 491 ule ratio of 0.375 yields the best prediction to the observed postseismic displacements with a
 492 misfit of $\bar{\chi}^2 = 31.2$ (Figure 13). The improvement in the Zener model over the Maxwell model
 493 can be clearly seen in the fit to the far-field data (Figure 7) where the Zener model does a sig-
 494 nificantly better job at explaining the transient rate of deformation throughout the five years
 495 considered in this study.

496 Because we are able to adequately describe the available five years of postseismic de-
 497 formation with a Zener model, we do not find it necessary to explore the parameter space for
 498 a more complicated Burgers rheology. However, since the Zener model is a Burgers model with
 499 an infinite steady-state viscosity, we can conclude that any Burgers rheology that has a trans-
 500 ient viscosity consistent with that found in Section 3.2 and a steady-state viscosity $\gtrsim 10^{20}$
 501 Pa s, which is effectively infinite on the time scale of five years, would also be able to sat-
 502 isfactorily describe the observable postseismic deformation.

503 The regularized inference of coseismic slip and afterslip for our preferred Zener model
 504 is shown in Figure 14. The inferred coseismic potency is 3.0×10^9 m³, equivalent to a Mw=7.26
 505 earthquake, and most of the slip is shallow and on the Sierra Cucapah fault segment. The po-
 506 tency of five years of afterslip is 1.1×10^9 m³. Most of the afterslip in our preferred model
 507 occurs within the first year after the earthquake and coincides with the location of our inferred
 508 coseismic slip. Inferred afterslip within the first year is accounting for the most rapid near-
 509 field transient deformation. After one year, afterslip is inferred to be deeper down on the Sierra
 510 Cucapah segment, which is describing much of the sustained near-field postseismic deforma-
 511 tion. We emphasize, that the GPS station closest to where we infer afterslip, P496, is still about
 512 30 km away, which is too far for us to conclusively argue for sustained localized deformation
 513



540 **Figure 14.** Inferred coseismic slip and afterslip when assuming a Maxwell rheology in the lower crust and
 541 a Zener rheology in the upper mantle. The transient viscosity η_K in the mantle and steady-state viscosity η_M
 542 in the crust are set equal to the effective viscosities from Figure 12. We set $\frac{\mu_K}{\mu} = 0.375$ in the upper mantle.

515 rather than shallow distributed deformation. The deep afterslip inferred after one year could
 516 potentially be describing deformation resulting from lower crustal flow. To test this, we have
 517 modified our preferred model by decreasing the lower crustal viscosity from 5.91×10^{19} Pa
 518 s to 1×10^{19} Pa s, which is still consistent with our viscosity inference from Section 3.2, and
 519 we inverted for fault slip. We find that a model with a weaker lower crust adequately describes
 520 the postseismic displacements without any afterslip after one year, while still requiring about
 521 the same amount of afterslip over the first year. We do believe that the early, shallow after-
 522 slip on the Sierra Cucapah segment is a robust feature in our preferred model, while we are
 523 not confident in our inference of later deep afterslip.

524 The postseismic displacements predicted by our preferred model are shown in Figures
 525 4, 5 and 7. Overall, the trends in the near-field and far-field transient deformation are accu-
 526 rately described. In particular, the trends in far-field deformation are much better described
 527 by our preferred Zener model than either an elastic model or a model with a Maxwell viscoelas-
 528 tic mantle (Figure 7). There are a few areas where we have notable misfit. Most of our mis-
 529 fit is for the near-field stations in the Imperial Valley, and we attribute this misfit to our rel-
 530 atively simple fault geometry, which does not account for potential fault slip in the Imperial
 531 Valley triggered by the El Mayor-Cucapah earthquake [Wei *et al.*, 2011a, 2015]. In particu-
 532 lar, we are unable to model the sustained, rapid rate of deformation at station P496, which sug-
 533 gests that this station could be influenced by a more localized deformation mechanism than
 534 is considered in this study. Additionally, we see systematic misfit in the later postseismic pe-
 535 riod west of the Landers and Hector Mine earthquakes, which may be the result of unmod-
 536 eled postseismic deformation resulting from those earthquakes. Lastly, there are clear discrep-
 537 ancies between the observed and predicted vertical deformation following the first year after
 538 the El Mayor Cucapah earthquake. We observe a broad uplift throughout Southern Califor-
 539 nia, which is inconsistent with any postseismic model.

543 **4 Discussion**

544 It has long been recognized that deep afterslip and viscoelastic relaxation following an
 545 upper crustal earthquake can result in similar horizontal ground deformation at the surface [e.g.
 546 *Savage*, 1990; *Pollitz et al.*, 2001; *Hearn*, 2003; *Feigl and Thatcher*, 2006]. The similarity of
 547 the horizontal postseismic deformation results in a non-uniqueness in inferences of afterslip
 548 or viscoelastic relaxation. In contrast, the spatial pattern of vertical postseismic deformation
 549 has been proposed to be a discriminant between deep afterslip and viscoelastic relaxation [e.g.
 550 *Pollitz et al.*, 2001; *Hearn*, 2003]. It is, however, important to note that patterns of vertical de-
 551 formation are very sensitive to the depth-dependence of viscosity below the upper crust [*Yang*
 552 and *Toksöz*, 1981; *Hetland and Zhang*, 2014]. The similarity between deformation resulting
 553 from deep afterslip and viscoelastic relaxation of coseismic stresses is different from the ill-
 554 posedness described in Section 3.2. In our method, any inferred afterslip will also mechani-
 555 cally drive additional viscoelastic relaxation. The horizontal deformation resulting from deep
 556 afterslip will generally be in the opposite direction as horizontal deformation resulting from
 557 viscoelastic relaxation of subsequent stresses in the lower crust (Figure 9). As a result, there
 558 is a trade-off between inferences of deep afterslip and lower crustal viscosity. In our synthetic
 559 tests in *Hines and Hetland* [2016], we have found that inverting surface deformation for af-
 560 terslip and viscosity within the same depth interval tends to result in overestimated afterslip
 561 and an underestimated viscosity.

562 Most postseismic studies assume Maxwell viscoelasticity in the lower crust and upper
 563 mantle [e.g. *Nur and Mavko*, 1974; *Pollitz et al.*, 2000; *Hetland*, 2003; *Freed et al.*, 2006; *John-*
 564 *son et al.*, 2009; *Hearn et al.*, 2009], which is the simplest viscoelastic rheologic model. In South-
 565 ern California, postseismic studies following the Landers [*Pollitz et al.*, 2000], Hector Mine
 566 [*Pollitz et al.*, 2001], and El Mayor-Cucapah earthquake [*Spinler et al.*, 2015; *Rollins et al.*, 2015],
 567 have assumed Maxwell viscoelasticity in the lower crust and upper mantle and have inferred
 568 upper mantle viscosities on the order of 10^{17} to 10^{18} Pa s and lower crust viscosities $\gtrsim 10^{19}$
 569 Pa s. These postseismic studies are consistent with *Kaufmann and Amelung* [2000] and *Cav-*
 570 *alié et al.* [2007], who found that an upper mantle viscosity of 10^{18} Pa s and a crustal viscos-
 571 ity $\gtrsim 10^{20}$ Pa s are necessary to describe subsidence resulting from changes in loading from
 572 Lake Mead. This isostatic adjustment is a process with similar spatial and temporal scales as
 573 postseismic deformation, and thus the inferred viscosities of these two types of studies would
 574 likely agree. While these studies found viscosities that are consistent with our effective vis-
 575 cosities from Section 3.2, they are inconsistent with viscosity estimates made from geophys-
 576 ical processes that occur over longer time scales. For example, *Lundgren et al.* [2009] found
 577 that lower crust and upper mantle viscosities on the order of 10^{21} and 10^{19} Pa s, respectively,
 578 are needed to describe interseismic deformation along the Southern San Andreas fault zone
 579 in the Salton Sea region. An even higher mantle viscosity, on the order of 10^{20} Pa s, is re-
 580 quired to describe isostatic adjustment resulting from the draining of Lake Bonneville, which
 581 occurs on the time scales of 10^4 years [*Crittenden*, 1967; *Bills and May*, 1987].

582 An additional deficiency with the Maxwell rheology is that it predicts a steady decay
 583 in the rate of postseismic deformation over time, which fails to describe the commonly ob-
 584 served rapid, early transience followed by a relatively steady rate of postseismic deformation.
 585 One could explain the early transient postseismic deformation with fault creep and the later
 586 phase with relaxation in a Maxwell viscoelastic lower crust and upper mantle [e.g. *Hearn et al.*,
 587 2009; *Johnson et al.*, 2009]. However, postseismic deformation at distances greater than ~ 200
 588 km from the El Mayor-Cucapah epicenter can only be attributed to viscoelastic relaxation [*Freed*
 589 *et al.*, 2007] and we have demonstrated that the far-field deformation cannot be explained with
 590 a Maxwell rheology (Figure 7).

591 We found that a Zener rheology in the upper mantle with a transient viscosity of $\sim 10^{18}$
 592 Pa s does a noticeably better job at predicting far-field postseismic deformation. A general-
 593 ization of the Zener viscoelastic model, schematically represented as several Kelvin elements
 594 connected in series, is commonly used to describe seismic attenuation [*Liu et al.*, 1976]. The
 595 highest viscosity needed to describe seismic attenuation is on the order of 10^{16} Pa s [*Yuen and*

596 *Peltier*, 1982] which has a characteristic relaxation time on the order of days. Even though
 597 our inferred transient viscosity is orders of magnitude larger than that required for seismic at-
 598 tenuation models, the two models are not incompatible. Rather, the delayed elasticity in seis-
 599 mic attenuation models occurs on such short time scales that it can be considered part of the
 600 instantaneous elastic phase of deformation associated with the preferred Zener model in this
 601 study.

602 Of course, a Zener rheology provides an incomplete descriptions of the asthenosphere,
 603 as it does not have the fluid-like behavior required to explain isostatic rebound or convection
 604 in the mantle [*O'Connell*, 1971]. *Yuen and Peltier* [1982] proposed a Burgers rheology with
 605 a low transient viscosity ($\eta_K \approx 10^{16}$ Pa s) and high steady-state viscosity ($\eta_M \approx 10^{21}$ Pa
 606 s) to describe both seismic attenuation and long term geologic processes. The justification of
 607 a Burger's rheology mantle is further supported by laboratory experiments on olivine [*Chopra*,
 608 1997]. *Pollitz* [2003] sought to describe postseismic deformation following Hector Mine with
 609 a Burgers rheology mantle and they found a best fitting transient viscosity of 1.6×10^{17} Pa
 610 s and steady-state viscosity of 4.6×10^{18} Pa s. While the Burgers rheology was introduced
 611 as a means of bridging the gap between relaxation observed in long and short term geophys-
 612 ical processes, the inferred steady state viscosity from *Pollitz* [2003] is still inconsistent with
 613 the Maxwell viscosities inferred from studies on the earthquake cycle and Lake Bonneville.
 614 The transient viscosity inferred by *Pollitz* [2003] is constrained by the earliest phase of post-
 615 seismic deformation following the Hector Mine earthquake. While *Pollitz* [2003] ruled out deep
 616 afterslip as an alternative mechanism based on inconsistent vertical deformation, it is still pos-
 617 sible to successfully describe all components of early postseismic deformation following the
 618 Hector Mine earthquake with afterslip at seismogenic depths [*Jacobs et al.*, 2002]. It is then
 619 possible that the preferred rheologic model from *Pollitz* [2003] was biased towards inferring
 620 a particularly low transient viscosity by neglecting to account for afterslip. This is in contrast
 621 to the present study, where we have inferred a viscosity structure simultaneously with after-
 622 slip. We also argue that a transient rheology is necessary to explain postseismic deformation;
 623 however, our preferred transient viscosity of $\sim 10^{18}$ Pa s in the upper mantle is an order of mag-
 624 nitude larger than the transient viscosity found by *Pollitz* [2003]. Since a Zener model is able
 625 to describe the available postseismic deformation following the El Mayor-Cucapah earthquake,
 626 any Burgers rheology with a steady-state viscosity that is $\gtrsim 10^{20}$ Pa s, effectively infinite over
 627 five years, would also be able to describe the postseismic deformation. Such a Burgers model
 628 might then be consistent with the steady-state viscosities necessary for lake loading, interseis-
 629 mic deformation, and mantle dynamics.

630 5 Conclusion

631 We have extracted a smoothed estimate of postseismic deformation following the El Mayor-
 632 Cucapah earthquake from GPS displacement time series. Our estimated postseismic deforma-
 633 tion reveals far-field (epicentral distances $\gtrsim 200$ km) transient deformation which is undetectable
 634 after about three years. Near-field deformation exhibits transience that decays to a sustained,
 635 elevated rate after about one or two years. We found that near-field transient deformation can
 636 be explained with shallow afterslip, and the sustained rate of near-field deformation can ei-
 637 ther be explained with continued afterslip or viscoelastic relaxation in the lower crust. Far-field
 638 transient deformation can be more definitively ascribed to viscoelastic relaxation at depths greater
 639 than ~ 60 km. Beneath that depth, a transient viscosity of $\sim 10^{18}$ Pa s is required to describe
 640 the rate of far-field deformation throughout the five years considered in this study. By describ-
 641 ing the available postseismic deformation with a transient rheology in the mantle, our preferred
 642 model does not conflict with the generally higher steady-state viscosities inferred from geo-
 643 physical processes occurring over longer time scales.

644 **Acknowledgements**

645 We thank Andy Freed for an illuminating discussion on the data used in this study. This
 646 material is based on EarthScope Plate Boundary Observatory data services provided by UN-
 647 AVCO through the GAGE Facility with support from the National Science Foundation (NSF)
 648 and National Aeronautics and Space Administration (NASA) under NSF Cooperative Agree-
 649 ment No. EAR-1261833. The data used in this study can be found at www.unavco.org. This
 650 material is based upon work supported by the National Science Foundation under Grant Num-
 651 bers EAR 1045372 and EAR 1245263.

652 **References**

- 653 Aagaard, B. T., M. G. Knepley, and C. A. Williams (2013). A domain decomposition
 654 approach to implementing fault slip in finite-element models of quasi-static and dy-
 655 namic crustal deformation, *Journal of Geophysical Research: Solid Earth*, 118, doi:
 656 10.1002/jgrb.50217.
- 657 Argus, D. F., M. B. Heflin, G. Peltzer, F. Crampé, and F. H. Webb (2005), Interseismic
 658 strain accumulation and anthropogenic motion in metropolitan Los Angeles, *Journal of*
 659 *Geophysical Research: Solid Earth*, 110(4), 1–26, doi:10.1029/2003JB002934.
- 660 Aster, R. C., B. Borchers, and C. H. Thurber (2011), Parameter Estimation and Inverse
 661 Problems, vol. 90, Academic Press.
- 662 Bawden, G. W., W. Thatcher, R. S. Stein, K. W. Hudnut, and G. Peltzer (2001), Tectonic
 663 contraction across Los Angeles after removal of groundwater pumping effects., *Nature*,
 664 412(August), 812–815, doi:10.1038/35090558.
- 665 Bills, B. G., and G. M. May (1987), Lake Bonneville: Constraints on Lithospheric Thick-
 666 ness and Upper Mantle Viscosity From Isostatic Warping of Bonneville, Provo, and
 667 Gilbert Stage Shorelines, *Journal of Geophysical Research-Solid Earth and Planets*,
 668 92(B11), 11,493–11,508, doi:10.1029/JB092iB11p11493.
- 669 Çakir, Z., S. Ergintav, H. Özener, U. Dogan, A. M. Akoglu, M. Meghraoui, and
 670 R. Reilinger (2012), Onset of aseismic creep on major strike-slip faults, *Geology*,
 671 40(12), 1115–1118, doi:10.1130/G33522.1.
- 672 Cavalié, O., M. P. Doin, C. Lasserre, and P. Briole (2007), Ground motion measurement in
 673 the Lake Mead area, Nevada, by differential synthetic aperture radar interferometry time
 674 series analysis: Probing the lithosphere rheological structure, *Journal of Geophysical*
 675 *Research: Solid Earth*, 112(3), 1–18, doi:10.1029/2006JB004344.
- 676 Cetin, E., Z. Çakir, M. Meghraoui, S. Ergintav, and A. M. Akoglu (2014), Extent and
 677 distribution of aseismic slip on the İsmetpaşa segment of the North Anatolian Fault
 678 (Turkey) from Persistent Scatterer InSAR, *Geochemistry, Geophysics, Geosystems*, 15,
 679 doi:10.1002/2014GC005307. Received.
- 680 Chopra, P. N. (1997), High-temperature transient creep in olivine rocks, *Tectonophysics*,
 681 279, 93–111, doi:10.1016/S0040-1951(97)00134-0.
- 682 Crittenden, M. (1967), Viscosity and Finite Strength of the Mantle as Determined from
 683 Water and Ice Loads*, *Geophysical Journal of the Royal Astronomical ...*, pp. 261–279,
 684 doi:10.1111/j.1365-246X.1967.tb06243.x.
- 685 Davis, J. L., B. P. Wernicke, and M. E. Tamisiea (2012), On seasonal signals in geode-
 686 tic time series, *Journal of Geophysical Research: Solid Earth*, 117(1), 1–10, doi:
 687 10.1029/2011JB008690.
- 688 Feigl, K. L., and W. Thatcher (2006), Geodetic observations of post-seismic transients in
 689 the context of the earthquake deformation cycle, *Comptes Rendus - Geoscience*, 338,
 690 1012–1028, doi:10.1016/j.crte.2006.06.006.
- 691 Fletcher, J. M., O. J. Teran, T. K. Rockwell, M. E. Osokin, K. W. Hudnut, K. J. Mueller,
 692 R. M. Spelz, S. O. Akciz, E. Masana, G. Faneros, E. J. Fielding, S. Leprince, A. E.
 693 Morelan, J. Stock, D. K. Lynch, A. J. Elliott, P. Gold, J. Liu-Zeng, A. González-
 694 Ortega, A. Hinojosa-Corona, and J. González-García (2014), Assembly of a large

- 695 earthquake from a complex fault system: Surface rupture kinematics of the 4 April
 696 2010 El Mayor-Cucapah (Mexico) Mw 7.2 earthquake, *Geosphere*, 10(4), 797–827,
 697 doi:10.1130/GES00933.1.
- 698 Freed, A. M., R. Bürgmann, E. Calais, J. Freymueller, and S. Hreinsdóttir (2006), Impli-
 699 cations of deformation following the 2002 Denali, Alaska, earthquake for postseismic
 700 relaxation processes and lithospheric rheology, *Journal of Geophysical Research: Solid*
 701 *Earth*, 111, 1–23, doi:10.1029/2005JB003894.
- 702 Freed, A. M., R. Bürgmann, and T. Herring (2007), Far-reaching transient motions after
 703 Mojave earthquakes require broad mantle flow beneath a strong crust, *Geophysical*
 704 *Research Letters*, 34, 1–5, doi:10.1029/2007GL030959.
- 705 Gonzalez-Ortega, A., Y. Fialko, D. Sandwell, F. A. Nava-pichardo, J. Fletcher,
 706 J. Gonzalez-garcia, B. Lipovsky, M. Floyd, and G. Funning (2014), El Mayor-
 707 Cucapah (Mw7.2) earthquake: early near-field postseismic deformation from In-
 708 Sar and GPS observations, *Journal of Geophysical Research*, 119, 1482–1497, doi:
 709 10.1002/2013JB010193.Received.
- 710 Hauksson, E., J. Stock, K. Hutton, W. Yang, J. A. Vidal-Villegas, and H. Kanamori
 711 (2011), The 2010 Mw 7.2 El mayor-cucapah earthquake sequence, Baja Califor-
 712 nia, Mexico and Southernmost California, USA: Active seismotectonics along the
 713 Mexican pacific margin, *Pure and Applied Geophysics*, 168(3918), 1255–1277, doi:
 714 10.1007/s00024-010-0209-7.
- 715 Hearn, E. H. (2003), What can GPS data tell us about the dynamics of post-seismic defor-
 716 mation ?, (2003), 753–777.
- 717 Hearn, E. H., S. McClusky, S. Ergintav, and R. E. Reilinger (2009), Izmit earthquake post-
 718 seismic deformation and dynamics of the North Anatolian Fault Zone, *Journal of Geo-
 719 physical Research: Solid Earth*, 114(August 2008), 1–21, doi:10.1029/2008JB006026.
- 720 Hetland, E. A. (2003), Postseismic relaxation across the Central Nevada Seismic Belt,
 721 *Journal of Geophysical Research*, 108(Figure 2), 1–13, doi:10.1029/2002JB002257.
- 722 Hetland, E. A., and G. Zhang (2014), Effect of shear zones on post-seismic deformation
 723 with application to the 1997 Mw 7.6 manyi earthquake, *Geophysical Journal Interna-
 724 tional*, 198, 259–269, doi:10.1093/gji/ggu127.
- 725 Hines, T. T., and E. A. Hetland (2013), Bias in estimates of lithosphere viscosity from
 726 interseismic deformation, *Geophysical Research Letters*, 40(16), 4260–4265, doi:
 727 10.1002/grl.50839.
- 728 Hines, T. T., and E. A. Hetland (2016), Rapid and simultaneous estimation of fault slip
 729 and heterogeneous lithospheric viscosity from post-seismic deformation, *Geophysical*
 730 *Journal International*, 204(1), 569–582, doi:10.1093/gji/ggv477.
- 731 Jacobs, A., D. Sandwell, Y. Fialko, and L. Sichoux (2002), The 1999 (Mw7.1) Hector
 732 Mine, California, Earthquake: Near-Field Postseismic Deformation from ERS Interfer-
 733 ometry, *Bulletin of the Seismological Society of America*, 92(May), 1433–1442.
- 734 Johnson, K. M., and P. Segall (2004), Viscoelastic earthquake cycle models with deep
 735 stress-driven creep along the San Andreas fault system, *Journal of Geophysical Research*
 736 *B: Solid Earth*, 109, 1–19, doi:10.1029/2004JB003096.
- 737 Johnson, K. M., R. Bürgmann, and J. T. Freymueller (2009), Coupled afterslip and vis-
 738 coelastic flow following the 2002 Denali Fault, Alaska earthquake, *Geophysical Journal*
 739 *International*, 176(3), 670–682, doi:10.1111/j.1365-246X.2008.04029.x.
- 740 Jónsson, S., P. Segall, R. Pedersen, and G. Bjornsson (2003), Post-earthquake ground
 741 movements correlated to pore-pressure transients, *Nature*, 424(July), 179–183, doi:
 742 10.1038/nature01758.1.
- 743 Kaufmann, G., and F. Amelung (2000), Reservoir-induced deformation and continental
 744 rheology in vicinity of Lake Mead, Nevada, *Journal of Geophysical Research*, 105(B7),
 745 16,341, doi:10.1029/2000JB900079.
- 746 Kroll, K. A., E. S. Cochran, K. B. Richards-Dinger, and D. F. Sumy (2013), Aftershocks
 747 of the 2010 Mw 7.2 El Mayor-Cucapah earthquake reveal complex faulting in the Yuha
 748 Desert, California, *Journal of Geophysical Research: Solid Earth*, 118(October), 6146–

- 749 6164, doi:10.1002/2013JB010529.
- 750 Lekic, V., S. W. French, and K. M. Fischer (2011), Lithospheric Thinning Beneath Rifted
751 Regions of Southern California, *Science*, 334(November), 783–787.
- 752 Liu, H.-P., D. L. Anderson, and H. Kanamori (1976), Velocity dispersion due to anelastic-
753 ity; implications for seismology and mantle composition, *Geophysical Journal Interna-*
754 *tional*, 47(1), 41–58, doi:10.1111/j.1365-246X.1976.tb01261.x.
- 755 Lundgren, P., E. A. Hetland, Z. Liu, and E. J. Fielding (2009), Southern San Andreas-San
756 Jacinto fault system slip rates estimated from earthquake cycle models constrained by
757 GPS and interferometric synthetic aperture radar observations, *Journal of Geophysical*
758 *Research: Solid Earth*, 114(2), 1–18, doi:10.1029/2008JB005996.
- 759 McGuire, J. J., and P. Segall (2003), Imaging of aseismic fault slip transients recorded
760 by dense geodetic networks, *Geophysical Journal International*, 155(3), 778–788, doi:
761 10.1111/j.1365-246X.2003.02022.x.
- 762 Meade, B. J., and B. H. Hager (2005), Block models of crustal motion in southern Cal-
763 ifornia constrained by GPS measurements, *Journal of Geophysical Research B: Solid*
764 *Earth*, 110, 1–19, doi:10.1029/2004JB003209.
- 765 Murray, J. R., and P. Segall (2005), Spatiotemporal evolution of a transient slip event on
766 the San Andreas fault near Parkfield, California, *Journal of Geophysical Research : Solid*
767 *Earth*, 110(9), 1–12, doi:10.1029/2005JB003651.
- 768 Nur, A., and G. Mavko (1974), Postseismic viscoelastic rebound, *Science*, 183(4121),
769 204–206, doi:10.1038/098448b0.
- 770 O'Connell, R. J. (1971), Rheology of the Mantle, *EOS, Transactions, American Geophysi-*
771 *cal Union*, 52, 140–142.
- 772 Oskin, M. E., J. R. Arrowsmith, A. Hinojosa Corona, A. J. Elliott, J. M. Fletcher, E. J.
773 Fielding, P. O. Gold, J. J. Gonzalez Garcia, K. W. Hudnut, J. Liu-Zeng, and O. J. Teran
774 (2012), Near-field deformation from the El Mayor-Cucapah earthquake revealed by
775 differential LIDAR, *Science*, 335(6069), 702–705, doi:10.1126/science.1213778.
- 776 Pollitz, F., C. Wicks, and W. Thatcher (2001), Mantle Flow Beneath a Continental Strike-
777 Slip Fault : Postseismic Deformation After the 1999 Hector Mine Earthquake, *Science*,
778 1814(2001), 1814–1818, doi:10.1126/science.1061361.
- 779 Pollitz, F. F. (2003), Transient rheology of the uppermost mantle beneath the Mo-
780 jave Desert, California, *Earth and Planetary Science Letters*, 215, 89–104, doi:
781 10.1016/S0012-821X(03)00432-1.
- 782 Pollitz, F. F., G. Peltzer, and R. Bürgmann (2000), Mobility of continental mantle: Evi-
783 dence from postseismic geodetic observations following the 1992 Landers earthquake,
784 *Journal of Geophysical Research*, 105(1999), 8035, doi:10.1029/1999JB900380.
- 785 Pollitz, F. F., R. Bürgmann, and W. Thatcher (2012), Illumination of rheological mantle
786 heterogeneity by the M7.2 2010 El Mayor-Cucapah earthquake, *Geochemistry, Geo-*
787 *physics, Geosystems*, 13(6), 1–17, doi:10.1029/2012GC004139.
- 788 Rauch, H. E., F. Tung, and C. T. Striebel (1965), Maximum likelihood estimates of linear
789 dynamic systems, *AIAA Journal*, 3(8), 1445–1450.
- 790 Riva, R. E. M., and R. Govers (2009), Relating viscosities from postseismic relaxation to
791 a realistic viscosity structure for the lithosphere, *Geophysical Journal International*, 176,
792 614–624, doi:10.1111/j.1365-246X.2008.04004.x.
- 793 Rollins, C., S. Barbot, and J.-P. Avouac (2015), Postseismic Deformation Following the
794 2010 M7.2 El Mayor-Cucapah Earthquake : Observations , Kinematic Inversions , and
795 Dynamic Models, *Pure and Applied Geophysics*, doi:10.1007/s00024-014-1005-6.
- 796 Savage, J. C. (1990), Equivalent strike-slip earthquake cycles in half-space and
797 lithosphere-asthenosphere earth models, *Journal of Geophysical Research*, 95, 4873,
798 doi:10.1029/JB095iB04p04873.
- 799 Savage, J. C., and J. L. Svart (2009), Postseismic relaxation following the 1992 M 7.3
800 Landers and 1999 M 7.1 Hector Mine earthquakes , southern California, *Journal of*
801 *Geophysical Research*, 114(B01401), doi:10.1029/2008JB005938.

- 802 Savage, J. C., J. L. Svarc, and S. B. Yu (2005), Postseismic relaxation and transient creep,
803 *Journal of Geophysical Research: Solid Earth*, 110, 1–14, doi:10.1029/2005JB003687.
- 804 Segall, P., and M. Mathews (1997), Time dependent inversion of geodetic data, *Journal of*
805 *Geophysical Research*, 102.
- 806 Spinler, J. C., R. A. Bennett, C. Walls, L. Shawn, and J. J. G. Garcia (2015), Assess-
807 ing long-term postseismic deformation following the M7.2 4 April 2010, El
808 Mayor-Cucapah earthquake with implications for lithospheric rheology in the
809 Salton Trough, *Journal of Geophysical Research: Solid Earth*, 120, 3664–3679, doi:
810 10.1002/2014JB011613.Received.
- 811 Wei, M., D. Sandwell, Y. Fialko, and R. Bilham (2011a), Slip on faults in the Imperial
812 Valley triggered by the 4 April 2010 Mw 7.2 El Mayor-Cucapah earthquake revealed by
813 InSAR, *Geophysical Research Letters*, 38(January), 1–6, doi:10.1029/2010GL045235.
- 814 Wei, M., Y. Liu, Y. Kaneko, J. J. McGuire, and R. Bilham (2015), Dynamic triggering of
815 creep events in the Salton Trough, Southern California by regional M5.4 earthquakes
816 constrained by geodetic observations and numerical simulations, *Earth and Planetary*
817 *Science Letters*, 427, 1–10, doi:10.1016/j.epsl.2015.06.044.
- 818 Wei, S., E. Fielding, S. Leprince, A. Sladen, J.-P. Avouac, D. Helmberger, E. Hauksson,
819 R. Chu, M. Simons, K. Hudnut, T. Herring, and R. Briggs (2011b), Superficial sim-
820 plicity of the 2010 El MayorCucapah earthquake of Baja California in Mexico, *Nature*
821 *Geoscience*, 4(9), 615–618, doi:10.1038/ngeo1213.
- 822 Yang M., and M. N. Toksöz (1981), Time-dependent deformation and stress relaxation
823 after strike-slip earthquakes, *Journal of Geophysical Research*, 86, 2889–2901.
- 824 Yuen, D. A., and W. R. Peltier (1982), Normal modes of the viscoelastic earth, *Geo-*
825 *physical Journal of the Royal Astronomical Society*, 69, 495–526, doi:10.1111/j.1365-
826 246X.1982.tb04962.x.